TAL TECH

SYNTHESIS-GROWTH AND CHARCTERIZATION OF FeS$_2$ PYRITE POWDERS FOR MONOGRAIN LAYER SOLAR CELL

PÜRIITSE FeS$_2$ PULBRI SÜNTEES-KASVATUS KASUTAMISEKS MONOTERAKIHT-PÄIKESEPATAREIDES

MASTER THESIS

Student:	Katriin Kristmann
Student code:	192603KAYM
Supervisors:	Dr. Taavi Raadik, Research Scientist
	Dr. Mare Altosaar, Lead Specialist

Tallinn, 2021

AUTHOR'S DECLARATION

Hereby I declare, that I have written this thesis independently.
No academic degree has been applied for based on this material. All works, major viewpoints and data of the other authors used in this thesis have been referenced.

21.05.2021

Author: ....
/signature /

Thesis is in accordance with terms and requirements

21.05.2021

Supervisor: …........................
/signature/

Accepted for defence

"......."...................20… .

Chairman of theses defence commission: Malle Krunks

/name and signature/

Non-exclusive licence for reproduction and publication of a graduation thesis[1]

I, Katriin Kristmann

1. grant Tallinn University of Technology free licence (non-exclusive licence) for my thesis "Synthesis-growth and charcterization of FeS_2 pyrite powders for monograin layer solar cell"

supervised by research scientist Dr. Taavi Raadik

1.1 to be reproduced for the purposes of preservation and electronic publication of the graduation thesis, incl. to be entered in the digital collection of the library of Tallinn University of Technology until expiry of the term of copyright;

1.2 to be published via the web of Tallinn University of Technology, incl. to be entered in the digital collection of the library of Tallinn University of Technology until expiry of the term of copyright.

2. I am aware that the author also retains the rights specified in clause 1 of the non-exclusive licence.

3. I confirm that granting the non-exclusive licence does not infringe other persons' intellectual property rights, the rights arising from the Personal Data Protection Act or rights arising from other legislation.

_____

21.05.2021

_____

Department of Materials and Environmental Technology
THESIS TASK

Student: Katriin Kristmann 192603KAYM

Study programme: Master of Materials and Processes for Sustainable Energetics

Main speciality: Materials for Sustainable energetics

Supervisor(s): Dr. Taavi Raadik, Research Scientist, +3726203210

Dr. Mare Altosaar, Lead Specialist, +3726203362

Thesis topic:

(in English)   Synthesis-growth and charcterization of FeS_2 pyrite powders for monograin layer solar cell

(in Estonian) Püriitse FeS_2 pulbri süntees-kasvatus kasutamiseks monoterakiht-päikesepatareides

Thesis main objectives:

1. Determining the synthesis-growth route for FeS_2 pyrite monograin powders

2. Characterizing the properties of synthesized powders for use in a monograin layer solar cell

3. Testing the first pyrite-based monograin layer solar cell and diode

Thesis tasks and time schedule:

No	Task description	Deadline
1.	Growing FeS_2 powders in two different fluxes and determining the suitable conditions for pyrite phase transition	30.05.2020
2.	Testing routes for pyrite powders doping and surface treatments	20.12.2020
3.	Experimenting with different junction partners for pyrite diodes and solar cells	25.03.2021
4.	Writing the thesis	21.05.2021

Language: English **Deadline for submission of thesis:** 21.05.2021

Student: Katriin Kristmann .....……......   21.05.2021

/signature/

Supervisor: Dr. Taavi Raadik   ……………………. ".......".....................2021

/signature/

Head of study programme: Dr. Sergei Bereznev   .... ".......".............2021

/signature/

CONTENTS

PREFACE

The topic of this thesis was initiated by my supervisor, research scientist Dr. Taavi Raadik. Precise focus to research FeS_2 pyrite for monograin layer solar cells was decided after an initial research into photovoltaic materials. The thesis is based on the experimental work carried out in the Laboratory of Photovoltaic Materials and in the Laboratory of Optoelectronic Materials Physics at the Department of Materials and Environmental Technology, Tallinn University of Technology (TalTech).

In this study, we put a lot of effort into designing the process route toward synthesis-growth of pyrite monograin powders. Although FeS_2 pyrite is a promising and desirable solar cell material, modest results have been achieved so far with efficiency of these solar cells. Our approach was to utilize pyrite in a monograin layer solar cell, that has its unique advantages before thin film or standard technology devices. Pyrite had not yet been researched for use in monograin layer solar cell technology.

As the author of this thesis, I am thankful for the opportunity to satisfy my scientific curiosity in the inspiring environment of our laboratory and help develop new technology toward a green energy revolution.

List of abbreviations and symbols

CB	conduction band		RT	room temperature
CBM	conduction band minimum		SEM	scanning electron microscopy
CIGSSe	$Cu(In,Ga)(S,S)e_2$		SILAR	successive ionic layer adsorption and reaction
CZTS	copper zinc tin sulfide		TCO	transparent conductive oxide
DFT	density functional theory			
DI	deionized		T_m	melting temperature
DSSC	dye-sensitized solar cells		V_0	built-in potential
EDX	energy-dispersive X-ray spectroscopy		VB	valence band
			VBM	valence band maximum
E_F	Fermi level		V_{liquid}	liquid volume
E_G	energy band gap		V_{OC}	open circuit voltage
FCC	face-centered cubic		V_{solid}	solid volume
$I\text{-}V$ curve	current-voltage curve		XRD	X-ray diffraction spectroscopy
MGL	monograin layer			
NC	nanocrystal		a	optical absorption coefficient
OPV	organic photovoltaics			
PCE	power conversion efficiency		Φ	work function
PV	photovoltaics			

INTRODUCTION

The world´s major energy sources are non-renewable, and their negative effects have brought our planet to a climate crisis [1]. These fossil fuels like oil, coal, and natural gas, that supply the ever-growing demand for energy, emit large amounts of carbon dioxide and other pollutant gases when they are being burned. These gases cause the well-known greenhouse effect, where the Sun's energy that has entered our atmosphere cannot escape it anymore. Temperature of the Earth has been rising and changing the global climate and ocean level, introducing unprecedented complications worldwide [1].

Because the amount of fossil fuels in the Earth's crust is finite, the depletion of these sources creates demand for alternative energy production. Main focus of research for relieving demand for fossil fuels has been on renewable energy. Sustainable energy is classified as energy that comes from resources that are constantly replenished, like sunlight, wind, geothermal heat, and rain. Solar energy in different forms is the source of nearly all energy on the earth and becomes a promising energy source as it does not produce any pollutants and is very widely available. In 2019, just over 2% of global electricity came from solar [2], while the European Commission has stated that by year 2050, 97% of electricity consumption must be from renewables [3]. That leads to believe the use of solar power is going to rise most, among other sustainable energy production solutions, with the demand for superior technology for solar cell devices.

There are many different technologies for solar cells production, most popular of which is based on single crystalline silicon, that holds nearly 80 % of market share [4], followed by multi-crystalline silicon and thin film solar cells. Thin film solar cells can be made from a variety of materials, including amorphous silicon, gallium arsenide (GaAs), cadmium telluride (CdTe), copper indium gallium diselenide (Cu(In,Ga)(S,Se)$_2$ and many more multinary compounds. Modern thin film solar cell technologies include also perovskite and organic material devices [4]–[6] Ideally, the materials for solar cells should be environmentally friendly, non-toxic, low-cost, and found in abundance in the earth crust.

In this study, FeS$_2$ in the pyrite crystal structure is investigated as an absorber material for monograin layer solar cell. FeS$_2$ has all necessary properties to be used in efficient solar cell devices, it has a suitable bandgap, high absorption coefficient and its constituent elements are non-toxic and available in the earth's crust abundantly. In addition, iron and sulphur are significantly cheaper to obtain and purify when comparing to silicon that is currently the most widely used solar cell material [7]–[9]. Monograin layer (MGL) solar cell technology is used for utilizing the pyrite absorber. The MGL solar

cell has a superstrate structure: graphite/absorber/buffer/TCO/substrate (glass or polymer film). Absorber for an MGL solar cell consists of a monolayer of nearly unisize, with a typical diameter of 50 μm, semiconductor powder crystals. The powders are synthesized at high temperatures in evacuated quartz ampoules starting from elemental or binary compound precursor materials in the presence of a flux material. FeS_2 powder crystals for the use in MGL solar cells or the synthesis conditions for FeS_2 monograin powders had not been studied yet. Overall aim of this research is to determine the suitable flux and synthesis-growth process for FeS_2 monograin powder production and investigate the properties of obtained powders and manufactured solar cell devices.

The thesis is based on the experimental work carried out in the Laboratory of Photovoltaic Materials and Laboratory of Optoelectronic Materials Physics at the Department of Materials and Environmental Technology, Tallinn University of Technology.

In Appendix 1, there is included a copy of the author's research article published on this thesis' topic.

1 THEORY AND LITERATURE REVIEW

One of the ways to lighten the demand for fossil fuels in energy supply is to utilize solar energy that reaches the Earth constantly and in abundance. There are many technologies to generate usable energy from solar energy, including solar heaters, plate and tube solar collectors, concentrating solar photovoltaic (PV) systems, and solar photovoltaic cells [4]–[6]. Solar PV or by simplified terms solar cells utilize the photovoltaic effect to generate electricity directly from solar irradiation. PV energy production is preferred by many users in industry and academic community for the solar cells have no moving parts, generate no noise or pollution while in use, and are considered durable and reliable [10]. The working principle and material properties of solar cell devices are described in the following chapters. The technological approach of this research and review of FeS_2 pyrite absorber material is described in the latter chapters of the theory segment.

1.1 Fundamentals of solar cells

The physical phenomenon that makes solar cell devices work is called the *photovoltaic effect,* which was first observed in 1839 by a French physicist, Edmund Becquerel [11]. The photovoltaic effect let the material to absorb incident solar irradiation and generates electron-hole pairs. These electron-hole pairs are charges that are free to move individually across the material. The material that allows this type of charge-creation is a *semiconductor*. Semiconductors are solid materials whose conductivities have values between conductors and insulators. Conventional solar cell contains a *p*-type semiconductor and an *n*-type semiconductor, which are arranged on top of each other, and finished with metal contacts on both sides to complete the circuit. *P*-type semiconductor material includes charge carriers that are mostly holes with a positive charge, whereas *n*-type semiconductor's main charge carriers are electrons with negative charges. After contacting *n*– and *p*-type semiconductors a junction is formed that is called a *p-n junction,* and built-in potential V_0 builds up due to the charge difference between the types of materials. When a light photon with an energy higher than the bandgap of semiconductor material is absorbed, the electrons and holes are freed. In contact with each other, the *p*-type material attracts a surplus electron from the *n*-type, that causes a flow of electrons through the circuit, also known as electricity. [5], [10]

For a semiconductor to have free charge carriers, the absorbed sunlight must raise an electron to a higher energy state from its lowest stable energy state. It is important to note the discrete energy levels that form for electrons, when an atom is in a crystal lattice [4], [10]. When the electron is bound to its atom, it is at a low energy state. The highest bound electron energy state of an atom in a crystal structure is called the valence band (VB) maximum. When the electron absorbs energy from a light photon, it is excited to a higher energy state where it is free to move in crystal lattice and is not bound to its atom. That higher energy levels of individual atoms of a semiconductor form an allowed energy band, that is called the conduction band (CB). The electron of a semiconductor is not able to attain energy states intermediate to these distinct energy levels. Between these two allowed energy levels lies the band gap (E_G), band gap is bordered by the valence band maximum and the conduction band minimum. Band gap energy is the minimum amount of energy that an electron must attain to be freed from the valence band and enter the conduction band to participate in electrical conduction. The energy band alignment is described in Figure 1.1. Excitation of an electron into the conduction band leaves behind a vacancy that is known as a hole. A hole has a positive charge and is also free to move across the material. The number and mobility of these free charge carriers is essential to characterize the conductivity of semiconductor materials and electronic devices.[12]

To understand the difference between *n*-type and *p*-type semiconductors, one must look at the energy band diagrams, that are depicted on Figure 1.1. [12], [13]. For an *n*-type semiconductor there is a donor level of electrons just below the conduction band. That introduces additional energy states for the electrons to jump into the conduction band and participate in conduction. For the *p*-type semiconductor, the additional energy states, called the acceptor states, are just above the valence band and while they host electrons, the holes that are left behind by the excited electrons participate in the *p*-type conductivity.
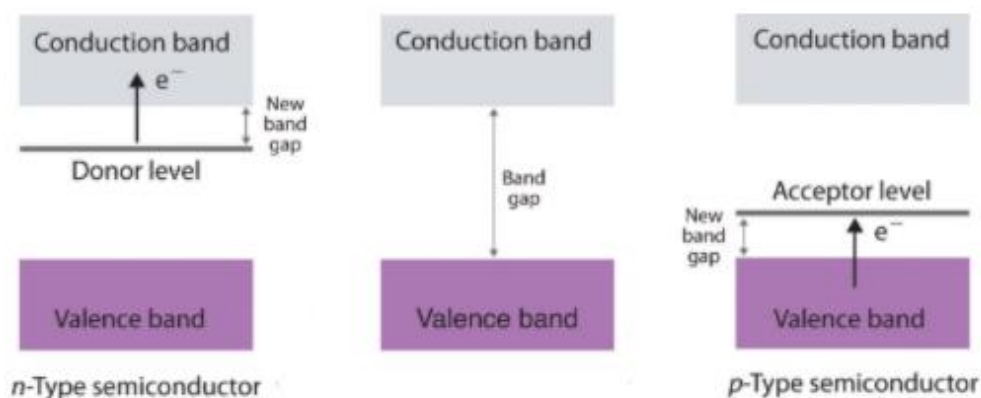
Figure 1.1. Energy band diagram of semiconductor [12]

The energy bands alignment with the Fermi level plays a role at the *p-n* junction formation. The Fermi level (E_F), which is an energy level inside a semiconductor's bandgap, is the highest energy level that is filled with electrons at absolute zero temperature (0 K)[13]. For *p*-type material it lies just above the valence band (below acceptor level) and for *n*-type material it lies below the conduction band (above donor level). When *p*- and *n*-type materials are arranged together, the Fermi levels align. The alignment causes *band bending* in energy diagram of materials at the interface between two semiconductors [10]. The energy diagram and a schematic of the *p-n* junction is depicted on Figure 1.2. When the two materials are joined together and Fermi levels are aligned, the free electrons in the *n*-type semiconductor near to the junction diffuse to the *p*-type semiconductor. At the same time, the mobile holes in the *p*-type semiconductor near to the junction diffuse to the *n*-type semiconductor [13]. After a while, the atoms near the interface in *n*-type material ionize and are positively charged. At the same way, the atoms near the interface in *p*-type material become negatively charged. The total region of the charged atoms in both sides is called *space-charge region*. In this region, an *electrical field* is created due to voltage difference that occurs between *n*-type and *p*-type materials. The electric field between the semiconductors causes a diffusion current from the *n*-type semiconductor through the electrical circuit to the *p*-type semiconductor, resulting in current flow.

Figure 1.2. Schematic of the *p-n* junction and energy band diagram [13]

1.1.1 Absorber materials in solar cells

The absorber material of the solar cell is where the solar irradiation is absorbed, and electron-hole pairs are created [10]. For that there is huge attention on the quality of the absorber layer. A perfect solar cell absorber should be a semiconductor material with a direct band gap of E_G = 0.9–1.5 eV, to match the energy quanta of the solar spectrum [14]. In addition, the absorber material sh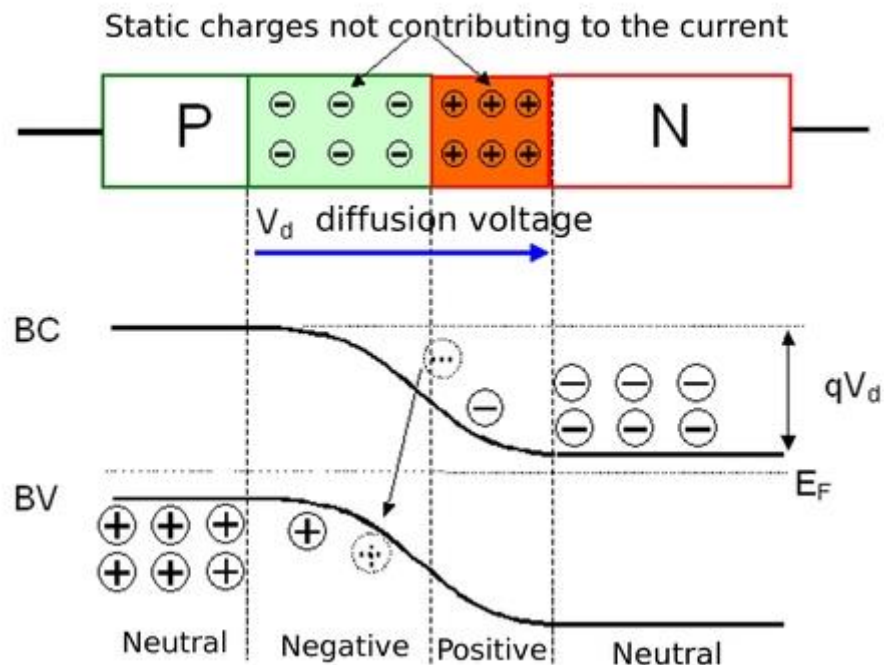ould have a high optical absorption coefficient ($\alpha > 10^4$ cm^{-1}) to provide a high number of excited charge carriers. The absorption coefficient determines how deep certain wavelengths of photons can penetrate in the material before being absorbed [6]. This determines the necessary absorber material thickness. In addition, a low recombination velocity between electrons and holes is desired, with the ability to form a good electrical junction with the buffer layer [10]. It is very important that the absorber material is environmentally nontoxic and available in abundance to honor the above goal of energetic sustainability.

Different semiconductor materials have been used as solar cell absorber layers. Crystalline silicon is the most common absorber material in today's commercial solar cell market [15]. This technology was introduced as early as 1954, by researchers at Bell Laboratories [16] who demonstrated the first practical silicon solar cell. Both mono-crystalline and poly-crystalline silicon are being widely used with the difference being in price and efficiency: mono-crystalline silicon production is expensive and wastes a lot of material but has a higher power conversion efficiency (PCE) reaching 26% when compared to poly-crystalline silicon solar cells (PCE 16%) [17], [18]. The photovoltaic cells that are wafer based and made from relatively thick materials (hundreds of μm) are named the *first-generation solar cells*. The first-generation technologies and devices have reached such maturity that over 80% of the solar market is dominated by silicon-based technology (Figure 1.3). However, alternative technologies have been developed to improve photoconversion efficiencies and to reduce the production cost of materials and devices.
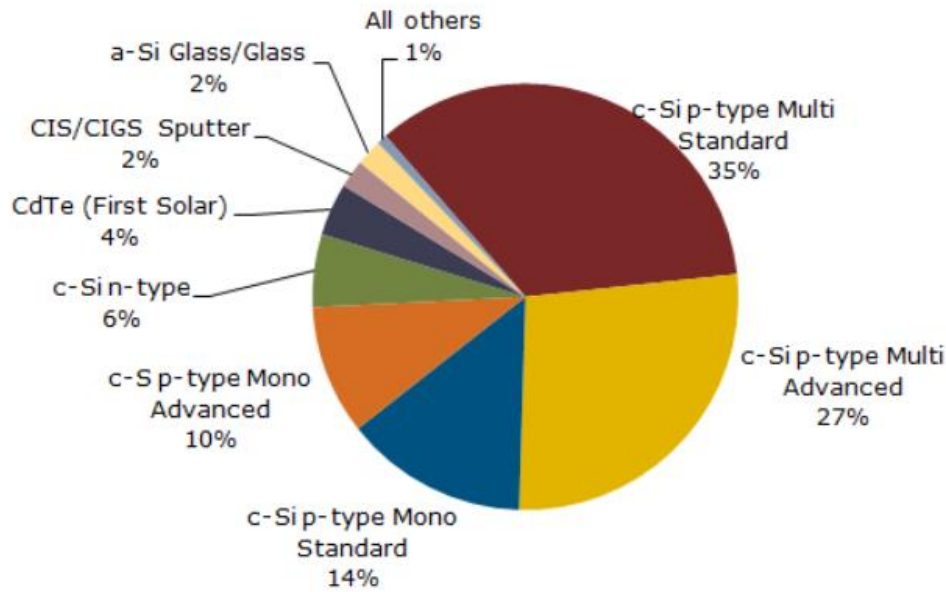
Figure 1.3. Solar PV module production by technology [15]

The second-generation solar cells are thin film photovoltaic cells that include semiconductor compound materials such as CdTe, GaAs and $CuIn_xGa_{(1-x)}(S_ySe_{1-y})_2$ (CIGSSe) [4]–[6]. The main advantage of using thin film solar cell technology is decreasing the amount of materials needed and the production cost significantly, while not making reductions in efficiency, because useful part of solar energy is absorbed already in the first 1 μm of material. The thin film solar cell industry also employs amorphous silicon thin film technology. The CdTe and CIGSSe devices have reached commercial production and efficiencies of 22% and 23% respectively [18], [19]. Even larger PCE has been attributed to GaAs cells, reaching 29 and 30%. However, there are environmental concerns with these materials since cadmium and tellurium, as well as arsenic are toxic elements that could harm the environment. Another problem occurs about indium and gallium in CIGSSe and GaAs cells, as the use of rare-earth elements in the production of commercially available devices is not possible for the rarity and high cost of elements.

The third-generation of solar cells has been emerging for few recent years. This includes organic photovoltaics (OPVs), copper zinc tin sulfide (CZTS) also known as kesterite solar cells, perovskite solar cells, dye-sensitized solar cells (DSSCs), and quantum dot solar cells [18], [20]. Technologies for solar cell manufacturing have advanced as well, including uses of nanotechnology and multijunction solar cells. Even though the third-generation cells have not yet reached maturity and affordability for commercial use, they have promising assets such as non-toxicity of CZTS, organic and perovskite compounds and abundance of constituent materials. However, the efficiencies remain

at 12% for kesterites, 13% for organic and over 21% for perovskite, but with low durability [18].

1.1.2 FeS$_2$ properties and crystal structure

FeS$_2$ in the crystalline form of pyrite is a promising candidate for solar cell absorber and has been explored for thin film solar cells, but the research has lately been impeded after little progress. FeS$_2$ or pyrite (henceforth used as synonyms) is promising for its suitable band gap at E_G = 0.95 eV, effective light absorption coefficient ($a > 10^5$ cm^{-1} for $hv > 1.3$ eV), an adequate minority carrier diffusion length (100-1000 nm) and an electron mobility up to 360 cm^{2}V^{-1}s^{-1} at room temperature [7], [21]–[23]. Iron and sulphur are present in the Earth's crust in abundance in different ores and sulphide minerals. Iron is mined extensively each year in gigaton scale and tons of material is disposed of as mining waste. Iron disulfide has a yellow-brass, metallic luster that is sometimes incorrectly recognized as gold. Due to this mistaken identity, it is often referred to as "fool's gold" [24]

FeS$_2$ offers possibilities of the lowest priced electricity production compared to other known solar cell materials. In a comparative study by Wadia et al. [8] a list of 23 solar cell materials were weighed against one another in terms of production cost (¢ per W) and annual electricity production potential (TW). FeS$_2$ was proven the best material in all these comparisons, outweighing Si in every aspect. Some key topics that favor FeS$_2$ over Si are: extraction cost ($1.70 per kg for Si vs $0.03 per kg for Fe), the energy input for extraction (24 kWh kg^{-1} for Si vs 2 kWh kg^{-1} for Fe), and a low levelized cost of the raw material per peak Watt (0.039 ¢ per W for Si vs <0.000002 ¢ per W for FeS$_2$). Taking the earth abundance and extraction cost into consideration, it was speculated that a 4% efficient FeS$_2$ solar cell could produce the electricity at the same price that of a 19% efficient Si solar cell [8].

Pyrite has a cubic crystal structure that resembles the fluorite structure (see Figure 1.4) [25]. It comprises of two interpenetrating cation (Fe^{2+}) and anion (S$_2^{2-}$) in face-centered-cubic (FCC) sublattices. The energy band diagram of pyrite on Figure 1.5 shows the positions of the valence band maximum (VBM) and conduction band minimum (CBM) relative to 0 eV at VBM. The energy bands have been calculated by Lehner et al. [26] using the quasiparticle self-consistent GW (QSGW) approximation. It can be seen from the energy diagram that the effective direct band gap of pyrite is indeed 0.95 eV.
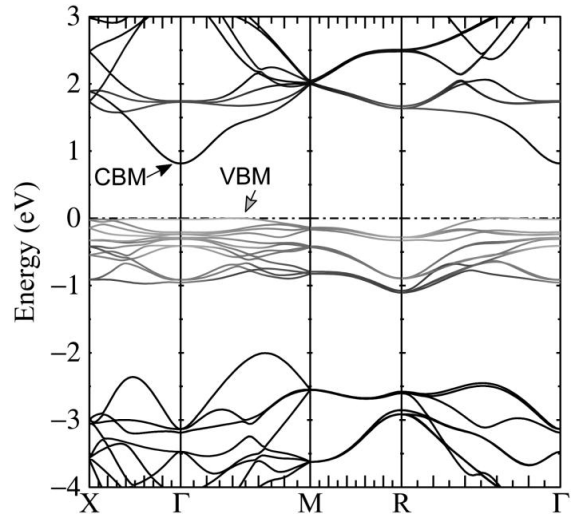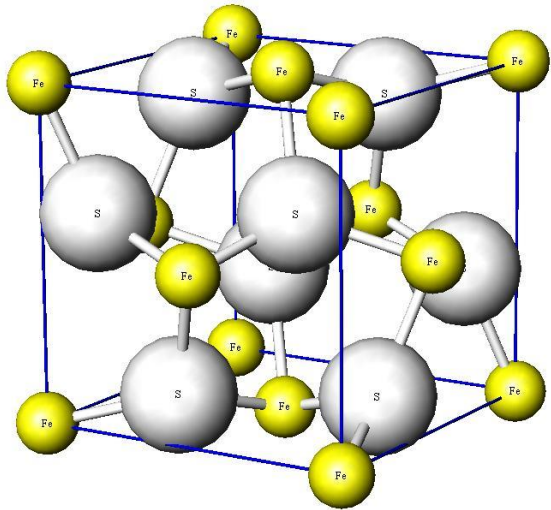
Figure 1.4. Crystal structure of cubic pyrite [25]   Figure 1.5. Pyrite energy band diagram [26]

The phase diagram of Fe – S system seen on Figures 1.6 and 1.7 and Table 1.1 reveal the conditions necessary to obtain the pyrite structure that is desired to benefit from above named material properties.
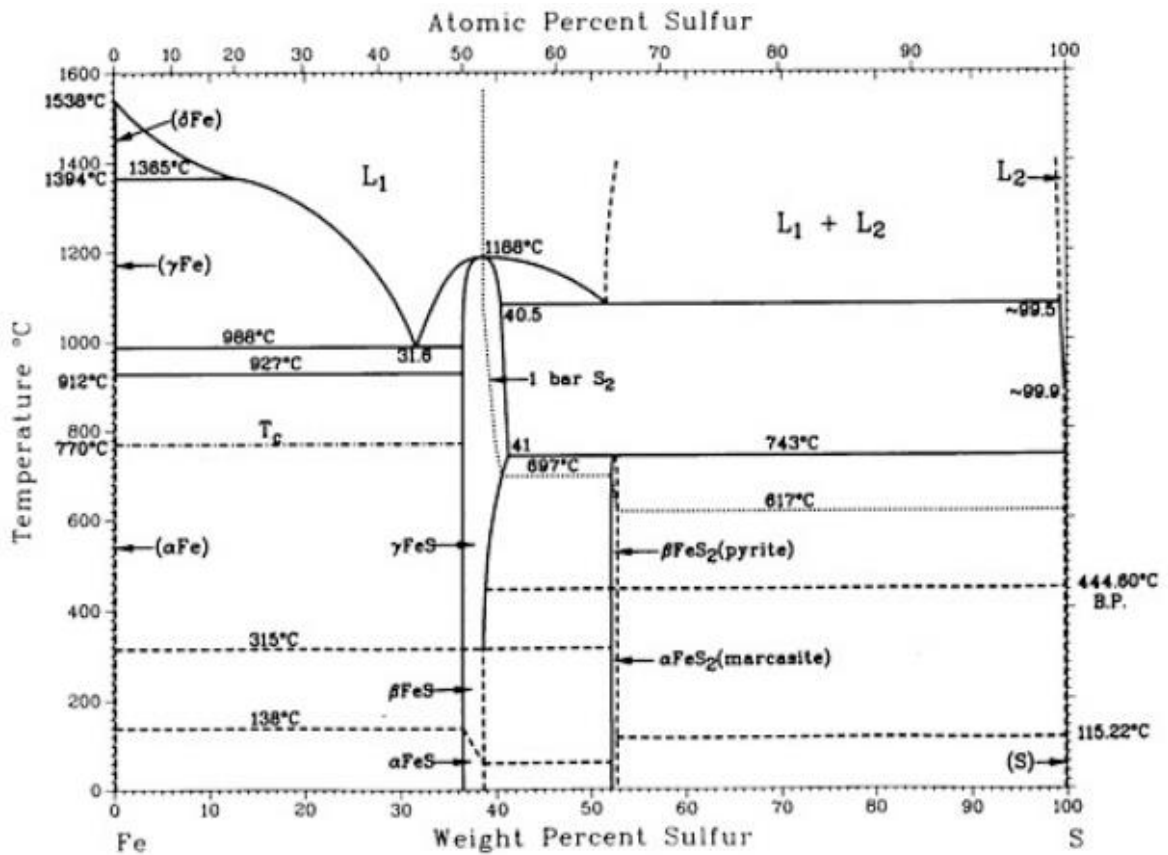
Figure 1.6. F-S phase diagram [27]

Table 1.1. Wt% composition of the Fe-S system compounds [27]

			From [Kubaschewski]
Phase	Composition, wt% S	Pearson symbol	Space group
(δFe)	0 to ~0.14	$cI2$	$Im\bar{3}m$
(γFe)	0 to ~0.05	$cF4$	$Fm\bar{3}m$
(αFe)	0 to 0.019	$cI2$	$Im\bar{3}m$
γFeS	36.5 to 41	$hP4$	$P6_3/mmc$
βFeS	36.5 to ~38	$hP24$	$P\bar{6}2c$
αFeS	36.5 to ~38	...	...
βFeS_2	~53.5	$cP12$	$Pa3$
αFeS_2	~53.5	$oP6$	$Pnnm$
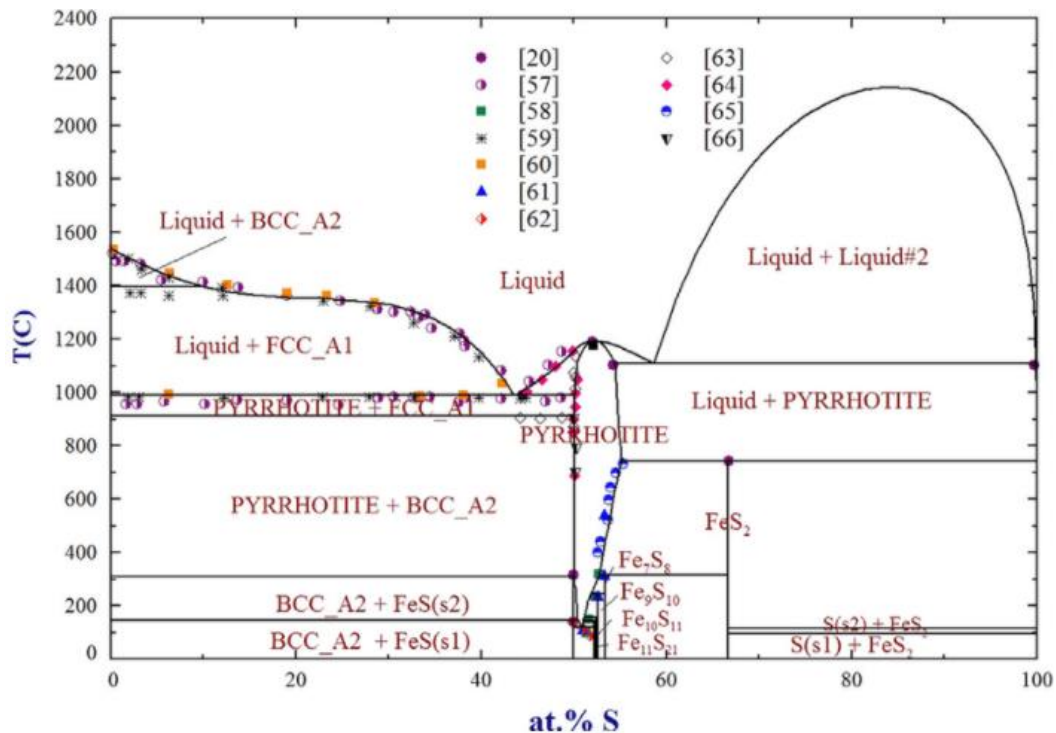
Figure 1.7. Fe-S phase diagram complementing parts from Figure 1.6 phase diagram [28]. References to the diagram can be found at the bottom of this page.[1]

[1] 20. T.B.Massalski(Ed.), BinaryAlloyPhaseDiagrams, Seconded., ASMInternational, MetalsPark,OH,1990

57. R. Loebe, E.Becker, The system iron-ironsulfide, Z.Anorg.Chem. 77(1912) 301–319

58. H. Nakazawa, N.Morimoto, Phase relations and superstructures of pyrrhotite, Fe$_{1-x}$S, Mater.Res.Bull.6 (1971) 345–358

59. K. Friedrich, Note on the melting diagram of the system FeS–Fe, Metallurgie 7 (1910) 301–319

60. K. Miyazaki, The equilibrium diagram of the iron and ironsulphide system, Sci. Rep. TohokuImp. Univ.Ser .I17 (1928) 877–882

61. F.GrØnvold, H.Haraldsen, On the phase relations of synthetic and natural pyrrhotites (Fe$_{1-x}$S), ActaChem.Scand. 6(1952) 1452–1469

62. G.H. Moh, G.Kullerud, Phase Relations at Low Temperatures: The Fe-S System, Carnegie Inst, Washington Yearbk 1964, pp.207

63. E. Jensen, Pyrrhotite: melting relations andcomposition, Am.J.Sci. 240 (1942) 695–699

64. W.Burgmann, G.Urbain, M.G.Frohberg, Contribution to the study of the System Fe-S in the region of iron sulfide (pyrrhotite), Mem.Sci.Rev.Met. 65 (1968) 567–578

65. R.G. Arnold, Pyrrhotite-Pyrite Equilibrium Relations between 325 and 745 °C (Ph.D Dissertation), Princeton University, United States, 1958

66. M. Nagamori, Technical note: compositions and free energies of Ag$_2$S and FeS saturated with metal, Can.Metall. Q.9 (1970) 531

The Fe–S system is characterized by the presence of several intermediate phases, some of which reveal semiconductor properties. Among this system there are $Fe_{1-x}S$, FeS, Fe_7S_8, Fe_9S_{10}, $Fe_{10}S_{11}$, $Fe_{11}S_{12}$, and FeS_2. α-FeS_2 marcasite is a semiconductor, and the phase appears at 115.22 °C below which the FeS_x composition exists in the flux of liquid sulphur. Marcasite turns into pyrite phase at 444.6 °C. There is another phase change at 617 °C [27] where pyrite decomposes. The decomposed phase constitutes pyrrhotite at 743 °C. According to [29] FeS_2 pyrrhotite melts at 1188 °C, exhibiting a broad homogeneity range toward excess S, and has two low temperature modifications such as β-$Fe_{1-x}S$ below 315 °C and α-$Fe_{1-x}S$ below 138 °C. According to [28] the monotectic reaction between the iron sulfide and sulfur-rich liquids occurs at 1082 °C and extends from 63 at% to 99.7 at% S. According to [27] the chemical composition of FeS_2 pyrite phase should be at least 53,5 wt% S. Below this proportion, the sulphur poor $Fe_{1-x}S$ phases start to show higher conductivity values that are not desirable for a photovoltaic absorber material [30]. Considering the multitude of phases and compositions, precise work is needed to obtain the single-phase pyrite absorber material with no secondary phases.

1.1.3 FeS₂ as absorber material in solar cell

The theoretical calculated efficiency limit (the Shockley–Queisser limit) for pyrite solar cells is 25% [21]. Since the first demonstration [7], despite high interest among material scientists and intermittent research efforts over three decades, FeS_2 solar cells never have exceeded a PCE greater than 3% [21]. This poor conversion efficiency is mainly the result of poor photovoltage, which has not exceeded 0.3 V. Secondary phases, surface conduction phenomena, and undesired doping have been reported [22], [23], [31], [32] as probable key issues behind this poor conversion efficiency. The lack of understanding has led to studies of the surface inversion, ionization of deep donor states and carrier tunneling [21].

When a FeS_2 surface is fractured, sulfur vacancies (S-vacancies) contribute to formation of the surface states. Significant concentrations of S-vacancies have been measured in pyrite faces by X-ray diffraction, photoelectron spectroscopy, and thermogravimetric data [9], [21]. According to density functional theory (DFT) calculations, the magnitude of the S-vacancies decays almost entirely to zero beyond approximately three atomic layers into the bulk [9]. The S deficiencies are argued to be from 1 at% up to 13 at%, that may turn the pyrite bandgap to zero by making the surface metallic (by conductivity). The small V_{OC} in FeS_2 solar cells has therefore been associated with S-

vacancies. The surface conductive layer is commonly assigned with a *p*-type behavior, while bulk is *n*-type [21].

Another way to advance the understanding of photovoltage loss, is a hole-rich inversion layer at the surface of pyrite photocells, that results in a leaky and/or small potential energy barrier [21], [31]. The low voltage might be caused by thermionic field emission (i.e., tunneling) through a thin potential barrier at the surface of the crystal, that is caused by a symmetry reduction due to change in iron coordination number. At the surface of a pyrite crystal Fe atoms are under-coordinated with five S atoms instead of the six S atoms octahedrally surrounding every Fe in the bulk lattice. The symmetry reduction leads to Fe 3d states to lose their degeneracy and split into surface states that lie within the band gap and the creation of surface states at energies close to the valence band edge. When the Fermi level of the *n*-type bulk tends to equilibrate with surface states, it creates a strong upward band bending and an inversion layer [9]. As a result, donors near the surface rise above the Fermi level and are ionized. This creates a thin potential barrier for direct tunneling of majority carriers. The leaky potential barrier can be a possible origin for the low V_{OC}. The carriers tunneling mechanism across the inversion layer is graphically explained on Figure 1.8. Both the S-vacancies and the reduction of Fe – S coordination create near-surface deep ionized donor states at the bulk of material [21], [33]. The donor states contribute to creating a sharp triangular potential barrier at the pyrite surface across which electrons tunnel.
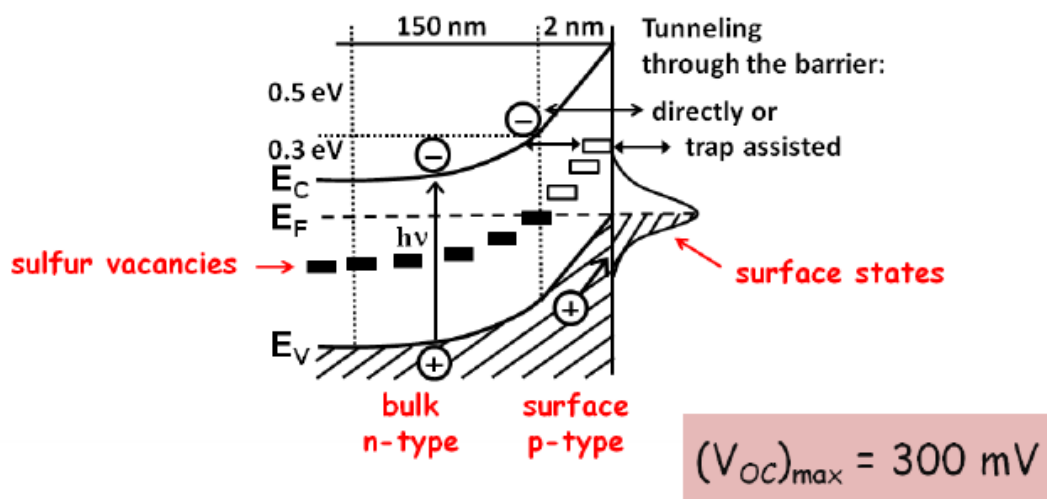
Figure 1.8. Thermionic field emission model of the pyrite surface based on Hall effect and UPS data of single crystals [33]. This model, which posits a thin inversion layer at the pyrite surface, may explain the low V_{OC} of pyrite devices

Table 1.2. Some of past works' achievements working with pyrite are represented in the following table

FeS₂ layer/solar cell technique	Conditions	Obtained phases, conductivity type	Doping	Results, comments	Ref.
Thin films. Sulfurization of sol-gel synthesized hematite (Fe_2O_3) films	550 ºC and pressures from 30.4 kPa (0.3atm) to 319.2 kPa (3.15 atm)	Pyrite, *n*-type	none	Low mobility of charge carriers. Stable photoresponse.	[22]
„Solar paint" from nanocrystals (NC)	Heating solvent-based dispersions up to 220 ºC	Pyrite, FeS and Fe_3S_4. *p*-type (estimated)	poly(3-hexyl-thiophene) (P3HT)	Very high conductivity, no photoresponse	[23]
FeS₂ NC dispersed in organic polymer	Different concentrations of FeS₂ NC in polymer P3HT	Pyrite, not specified	none	Good device stability, up to 3% PCE	[32]
Single crystal slabs grown by salt flux method	Wet junction in electrochemical cell, FeS₂ crystals etched in "Piranha solution"	Pyrite, *p*-type surface, *n*-type bulk	none	2.8 % PCE	[31]
Chemical Vapor Transport. *p-n* junction with sputtered ZnS	Pyrite-marcasite films sulfurized 4h 500 ºC	Pyrite, *p*-type	none	Rectifying junction, small photoresponse 0.0002% PCE	[31]
Spin coating with ink, with sputtered ZnS	Solution deposited, annealed in sulphur atm.	Polycrystalline pyrite, *p*-type	none	PCE 0.0014%	[31]
Single crystal	Chemical vapor transport, isothermal	Pyrite. Intrinsic *n*-type; phosphorus-doped *p*-type	None, or phosphorus-doped	carrier concentration 10^{16} cm^{-3}	[34]

It can be seen from the Table 1.2 that very different approaches have been adopted to deposit or grow pyrite films and crystals, with some techniques reaching efficiencies up to 3%. On the other hand, some researchers admit to continuously low rectification and photoresponse. Moreover, different growth techniques seem to yield either n-type or p-type conductivity for pyrite. It was analyzed by Linpensel [31] that thin film pyrite layers tend to show p-type conductivity, while single crystals and slabs show n-type conductivity, with a defect-dense surface layer that has been described before and can have different doping. Therefore, surface passivation was thought to be needed to lower carrier concentration to levels that can support a depletion region and to initiate an efficient charge separation.

1.1.4 Doping and surface treatments of FeS$_2$

It is widely accepted that FeS$_2$ pyrite may be unintentionally n doped by sulfur vacancies, especially on the surface of single crystals [35]. Doping is a common phenomenon for photovoltaic materials to vary the number of electrons and holes in semiconductors. It is commonly done by adding group V atoms to a group IV material, to increase the number of available electrons in the lattice and obtain a material that is n-type. Otherwise, adding group III atoms to group IV material will increase the number of holes present and create p-type doping [5], [6]. Because pyrite single crystals are predominantly n-type, whereas pyrite thin films are p-type, this material has been studied for different types of doping quite widely. Lehner et. al [36] has presented pyrite doping with Co and Ni to obtain n-type conductivity, while arsenic as dopant revealed intermittent results with alternating p and n type conductivities. Ruoshi Sun [37] and Willeke [34] have reported p-type conductivity of pyrite films caused by oxygen impurities and doping with phosphorus. Because a solar cell absorber layer is commonly with p-type conductivity [38]–[42], it can be useful to dope material to obtain this suitable conductivity type. As, P and O are group V and VI elements and could be used to experiment with p-type doping. Arsenic is toxic and does not comply with fundamental approach of this study. Alternatively, pyrite may also be successfully doped with another V group element, such as antimony (Sb), as is attempted in this research as well.

Pyrite films and crystals have been reported for significant surface defects and surface inversion layer [21], [23], [43], [44] that can cause tunneling of charge carriers across the interface and cause the low voltage of pyrite photocells. Their removal could be the

remedy for the low photoconversion and low V_{OC} of devices. One option to passivate the non-stoichiometric and defective surface is to deposit encapsulating layers that chemically bond to surface sulphur atoms, leading to a more perfect epitaxial interface [44]. ZnS, ZnO and SiO_2 have been experimented with notable success in surface passivation. Another useful approach is trying to remove the defected surface by chemical etching and sulphur annealing [43]. Surface passivation has revealed success, with chemical etches substantially reducing the conductivity of the inversion layer. So called "Piranha solution" (3 parts of conc. H_2SO_4, 1 part of 30% H_2O_2 [31]) has been one suggested etchant that is reported [33], [43] to reduce surface acceptor density. Alternatively, annealing pyrite in concentrated sulphur vapor at elevated temperatures may introduce sulphur back into the pyrite lattice, leaving a more stoichiometric surface.

1.2 Monograin technology

Main technologies used today for manufacturing solar cells include single crystalline- and polycrystalline Si, also thin film technologies [4]. The method of growing large single crystal ingots of silicon with very high chemical purity yields high quality materials for single crystalline Si solar cells but is very expensive and energy intense [17]. In addition, cutting and shaping the ultra-thin wafers from the single crystal wastes material, nearly half of the ingot will be wasted as sawdust, which makes it a problematic approach. The polycrystalline Si cells on the other hand suffer from lower power conversion efficiency [4], [45]. Thin film solar cells, that have gained tremendous attention in recent years, do not waste so much material and there are various different deposition techniques available, but the films are near always polycrystalline. The disadvantage of polycrystalline materials is they have a high concentration of defects on the grain boundaries that act as recombination centers for the photogenerated charge carriers [45]. As an alternative, the monograin layer solar cell (MGL) technology [39], [40], [42] uses monograin powders instead of films or cut ingots. In the monograin layer (MGL) solar cell the powder crystals covered with buffer layer for *p/n*-junction are fixed as a single layer of parallelly contacted array of tiny solar cells. The main advantage of the MGL technology is the separation of the absorber material production and solar module formation. MGL is also a relatively cheap technology, reduces material waste and combines the advantages of superior electrical properties of monocrystalline materials and simplicity of module production.

1.2.1 Monograin powder growth

Monograin powders are formed in the process of isothermal heating of precursor materials in the presence of liquid phase of a suitable salt (flux) as solvent. The solvent or flux in an amount that assists to rise the repelling forces between solid particles that exceed the capillary contracting forces. In these conditions the formation and growth of separate grains is possible. The crystals (grains) grow larger to lower their surface area relative to the bulk, thus being energetically more favorable [39], [40], [42]. One grain is ideally one single crystal, or several single-crystalline blocks of material in a single grain. The growth process takes place at higher temperature than the melting point (T_m) of flux material and lower than T_m (or decomposition) of the synthesized compound. The flux material is chosen according to the T_m and its chemical nature. The flux must stay inert to the precursor materials and not react with them.

One key point in the monograin synthesis-growth process is the ratio of added flux volume to the volume of other precursors (for forming solid target compound) at the synthesis temperature. The amount of molten flux must be sufficient to accelerate the reaction between solid phase precursors in the phase of formation-nucleation of grains and afterwards to fill the free volume between the formed solid compound particles to avoid them from sintering together. The volume of liquid flux is considered for the high temperature process of grain growth that takes place in the liquid phase of flux. Usually, the flux and precursors are taken to form nearly equal volumes of liquid and solid phase at the synthesis temperature, or at least to fulfill the requirement $V_{liquid} \geq 0.6V_{solid}$ [39], [40], [42].

To assure the proper composition of grains the choice of precursors is critical. Stable monograin powders have been synthesized from elemental precursors or from binary or multinary compounds[38]–[40], [42]. FeS_2 can be synthesized from elemental Fe and S or from some iron sulphide. According to the phase diagram of Fe – S [27] 53.5 wt% S is necessary. The composition of precursors mixture should be calculated according to the stoichiometry. FeS and elemental S were utilized in the present experiments to synthesize FeS_2.

The synthesis and crystallization process time is chosen by consideration that a longer period normally produces larger grains. Duration between 90 hours and one week is common in monograin growth [38], [39]. Growth is enhanced by higher temperature. As the MGL solar cell technology utilizes a layer of unisize powder crystals and for the reason that the grains size distribution in the grown monograin powder follows the normal (Gaussian) distribution, the powders were sieved into different size fractions after the removal of flux. A suitable fraction size for MGL is between 56-95 µm [38].

The remaining part of the synthesized powders can be recrystallized and used again, which minimizes the material loss significantly. Sieving analysis is used to describe the growth of particles' size. The median particle size d_m increases with growth duration t and temperature T as follows [38]:

$$d_m = At^{1/n} exp(-E_d \, / \, kT), \tag{1.1}$$

where A is a constant for a given flux and compound, k is the Boltzmann constant, T is the growth temperature, E_d is the activation energy of linear crystal growth and n is the geometric factor of growth mechanism. It enables to use the equation 1.1 to describe the grain growth mechanism.

1.2.2 Flux materials

Inorganic molten salts have proven to be suitable to support the synthesis and recrystallization. Good flux material needs to have low T_m, low vapor pressure and high solubility in water to be easily removed afterwards. The flux also cannot react with the precursors. For the synthesis of FeS_2 several flux materials can be used. At $T = 617$ ºC pyrite structure changes into FeS_2 of pyrrhotite structure that decomposes at $T = 743$ ºC (see Fig. 1.6). Therefore, the salts melting higher than 743 ºC are not usable. Different halide salts like KI, CdI_2, NaI have been used for monograin growth of kesterites [40], [41], but CdI_2 is found to react with precursors. That leaves the choice to use KI or NaI for pyrite grain growth at higher temperature region, where flux melts and pyrrhotite exists, and lower the temperature later to initiate phase change into pyrite. Another route is to synthesize FeS_2 in one of its natural constituents, liquid sulphur flux. It must also be noted that the constituents of used flux salt always dissolve in the formed compound at the level of their saturation at the growth temperature and can act as n- or p-type dopants and must be considered in the characterization. [38]. The solubility of different ions into the pyrite lattice by liquid flux growth has not been thoroughly studied before.

1.2.3 Monograin membrane solar cell

The MGL solar cell consists of a monolayer of monograin powder crystals of a narrow granulometric fraction, fixed with an organic resin (epoxy) [38]. After polymerization of

the resin, buffer layer that creates the *p-n* junction is deposited onto crystals' surfaces. Intrinsic zinc oxide layer and transparent conductive ZnO:Al layer (TCO) are deposited onto absorber/buffer structure to finish the cell., The thin layer of intrinsic ZnO prior to the conductive ZnO:Al acts as an insulator in case there are any pinholes or cracks in the buffer layer, both layers are deposited by RF sputtering. Indium or silver stripes are deposited on the TCO to serve as a front contact. Next the structure is glued onto a glass substrate. The back areas of crystals that were originally inside the epoxy are opened by etching the epoxy with H_2SO_4 and by additional abrasive treatment. Back contacts are made using graphite paste that finishes the solar cell structure (Figure 1.9).
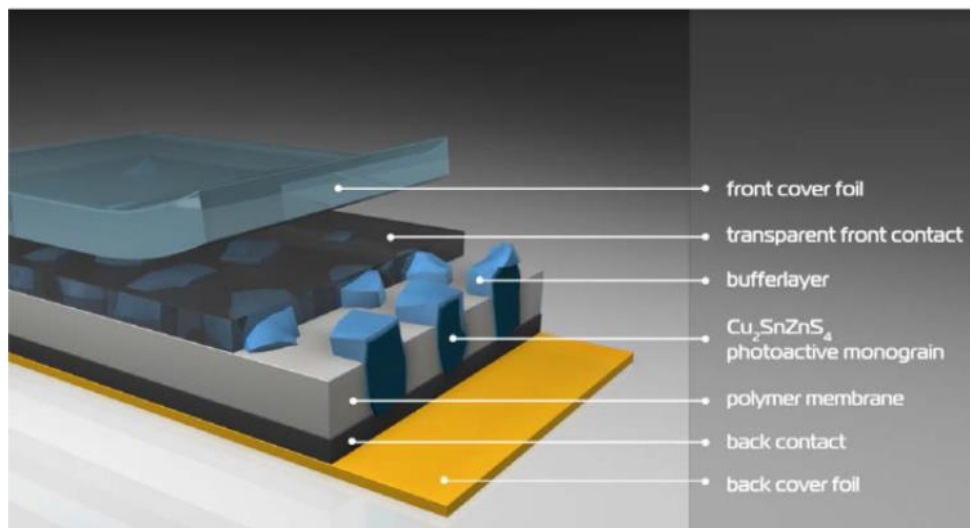
Figure 1.9. The schematic of MGL solar cell based on Cu_2SnZnS_4 (could be also pyrite) as the photoactive monograin [46]

MGL combines the advantages of high photoelectrical parameters of monocrystalline solar cells and lower cost of polycrystalline thin film solar cells. MGL solar cells can be flexible, they are lightweight, and it is possible to have no material losses, as the unused size fractions can be recrystallized to obtain new size distributions. MGL technology allows the formation of absorber layer separately from module fabrication which adds more flexibility to processing techniques. Schematic model of the MGL solar cell production can be seen in Figure 1.10. There are some disadvantages to the technology as well. Not all the solar cell area is working actively, there are empty spaces between the crystals, that is lost area for energy conversion. Size of the lost area depends on the packing density of crystals in the epoxy layer, which is related with microcrystals geometry. The upmost surface of the grains always needs special attention as the interfaces between the absorber and the buffer layer are key in the junction formation and defects there can become fatal to the solar cell. The surface passivation and treatments of grains may include chemical etching and thermal annealing. [38], [42]

26
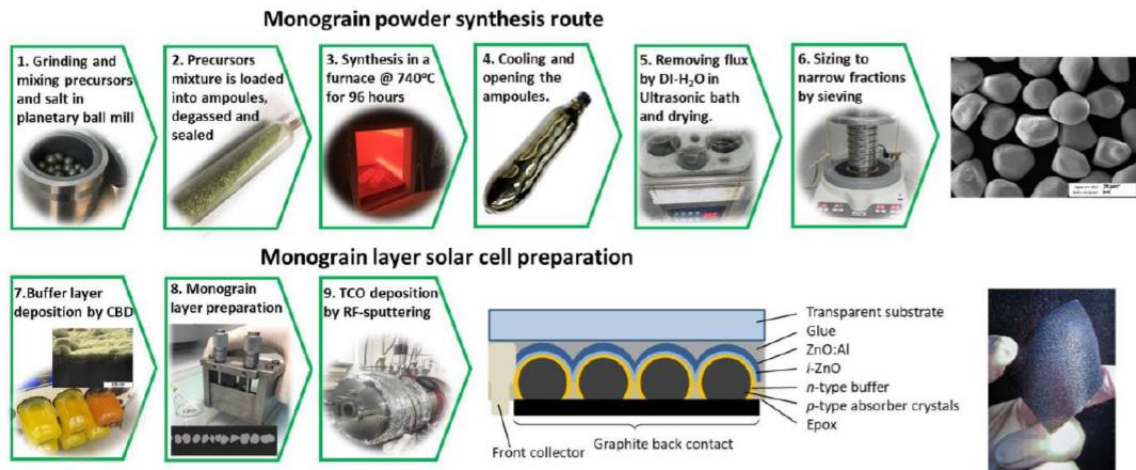
Figure 1.10. Monograin powder synthesis route [40]

1.3 Summary of the literature review and aim of the study

- Solar energy as a clean renewable energy source is gaining popularity as an alternative to harmful fossil fuels. Currently the PV market is dominated by silicon-based expensive and wasteful technologies. Very promising second-generation thin film solar cells use much less materials and offer alternatives to Si. Constituents of the thin film PV materials include rare earth elements of In and Ga, and toxic element like As, Te and Cd, making them expensive and problematic for commercial use. The development of new PV technology that is cheap and uses earth-abundant non-toxic elements would alleviate the pressure from the silicon and thin film PV industries.

- FeS_2 in the pyrite crystal structure seems to be a nearly ideal absorber layer for scalable thin solar cells due to its suitable band gap at $E_G = 0.95$ eV, high absorption coefficient, good minority carrier diffusion length, practically infinite elemental abundance, and low toxicity. It is recognized as cheap material, having several times lower extraction cost and energy input for extraction when compared to silicon. However, usage of pyrite as absorber material in solar cells is a big challenge. Although large short-circuit photocurrent densities (> 30 mA

27

cm^{-2}) have been reported from pyrite single crystals, all pyrite cells to date suffer from a low open-circuit voltage (V$_{OC}$) that limits their power conversion efficiency to ~3%. Proposed explanations for the low V$_{OC}$ include bulk phase impurities, a high concentration of bulk point defects (particularly sulphur vacancies), and a metallic FeS-like surface layer. The surface states generate a hole-rich surface inversion layer that possibly has a reduced band gap compared to the pyrite bulk and enables photogenerated electrons to tunnel through the very thin potential barrier at the surface of the crystal. If these obstacles can be overcome, FeS$_2$ will have the potential to dominate the commercial PV market, having its theoretical efficiency at 25%. Anyway, if challenges of pyrite's material remain, it has been speculated that a 4% efficient FeS$_2$ solar cell could produce the electricity at the same price that a 19% efficient Si solar cell.

- MGL technology developed in Taltech has advantages in comparison with thin film technologies, such as lower cost, minimal waste of materials and simplicity of technology. It also employs the advantage of using monocrystalline materials in the absorber layer, that have superior photoelectrical properties to polycrystalline ones. Fabrication of absorber material for MGL separately from making the whole structure of solar cell allows to use high temperatures and chemical treatments for the absorber material without affecting the device. So far, MGL solar cell technology is not used for producing pyrite solar cells.

- Single-phase pyrite that is of interest exists in the temperature region of 444 to 617 ^{o}C and has narrow compositional deviation from stoichiometry. At $T = 617$ ^{o}C, the FeS$_2$ pyrite structure transforms into pyrrhotite that in turn decomposes at $T = 743$ ^{o}C. Electrical and PV properties of pyrite are very sensitive to the sulfur deficiency as sulfur vacancy (Vs) is the prevailing defect. Therefore, the properties of single-phase pyrite can be tuned in a narrow area of temperatures and compositions on the Fe – S phase diagram. These circumstances limit the monograin powder growth temperature and the choice of flux material. Therefore, in the present study sulphur and KI were chosen as flux materials. Sulphur provides the abundance of it in pyrite, but due to high sulphur vapor pressure the process temperature is limited. KI as flux is used before for monograin powder growth of different materials. KI, melting at $T_m = 686$ ^{o}C, allows the growth of FeS$_2$ in the pyrrhotite structure. Therefore, the technological procedure for the phase transformation of FeS$_2$ into pyrite structure has to be found out and guaranteed. As below 444 ^{o}C the stable phase of FeS$_2$ is marcasite, the quenching of high temperature powder samples must be the only way to maintain the pyrite structure of FeS$_2$ monograins.

28

- Suitable flux material, that initiates the reaction and growth of monograin powders, as well as the synthesis time and temperature influence the size and morphology of produced powder crystals. The size and shape of monograin powder crystals is essential to MGL solar cell because the absorber layer consists of narrow granulometric fraction of crystals. Therefore, the adjustment of synthesis conditions increases the yield of usable powder fractions.

The overall aim of the study Based on the summary of literature the overall aim of the present study is to develop a process to synthesize FeS_2 pyrite monograin powder crystals, that are suitable to use in monograin membrane solar cells. For this purpose:

➢ FeS_2 monograin powders are synthesized and crystallized using FeS and S as precursors for the reaction in the liquid phase of S and KI as growth media. The morphology, size, elemental and phase compositions of powders are studied;

➢ FeS_2 crystals with suitable preliminary properties are used in the preparation of monograin membranes. Electrical properties are assessed from fabrication and characterization of different Schottky diodes;

➢ MGL solar cell with FeS_2 pyrite absorber layer and NiO buffer layer is fabricated and characterized on the basis of MGL solar cell technique;

➢ For NiO buffer layer deposition by SILAR method, the NiO thin films deposited on glass substrates are characterized by SEM, EDX and optical measurements.

2 EXPERIMENTAL

In this study FeS$_2$ monograin powders were synthesized from high-purity FeS and S acquired from Alpha Aesar (5N purity) using S and KI as liquid flux media. All syntheses were proceeded in evacuated quartz ampoules. Different synthesis times and temperatures were tested for these two fluxes to demonstrate the best technique for pyrite monograin growth. First part of this chapter will address the experiments in S flux. It appeared evident that liquid sulphur is not suitable for this process. Later powder growth experiments in KI flux proved more successful and additional work was done to improve on the powders synthesized in KI medium.

Due to the fact that the synthesis-growth of FeS$_2$ for monograin powder production was not used before, in the present study the syntheses were made stepwise, carefully testing the probable technical opportunities. In the very beginning of the synthesis-growth tests, the used quartz ampoules broke in the cooling down period. We found that the braking of ampoules could be avoided if the inside surfaces of quartz ampoules were covered by a carbon layer. The scheme of the following experimental steps in the frame of FeS$_2$ monograin powder synthesis-growth is presented in Figure 2.1.

Powder preparation

Synthesis-growth in S at T=500° C
T=550° C
T=600° C

Recristallization in KI at T=740° C
T= 720° C

Synthesis-growth from precursors FeS and S in KI   T=720° C

Result: Small and ununiformly shaped powders
Difficult to remove excess S

Conditions: bringing T down to 575° C for phase transition to pyrite

720 °C 680 h

200 °C 24 h

575 °C 6 h

Sample temperature regime

Result: Simpler to remove KI
More suitable powders achieved
No explosions during syntheses when carbonizing ampoules' inner surface and slowing T change

Post-treatments

Doping with Sb in recrystallization with Sb-KI flux   Result: *n*-type

Annealing in S saturated vapor pressure to relieve S defects   Result: *n*-type

Etching powders' surface with Piranha solution

***p-n* junction**

SILAR deposited NiO as *p*-type buffer layer

Characterization

Powders: - SEM
- EDX
- Raman
- XRD
- hot probe
Devices: *I-V* measurement
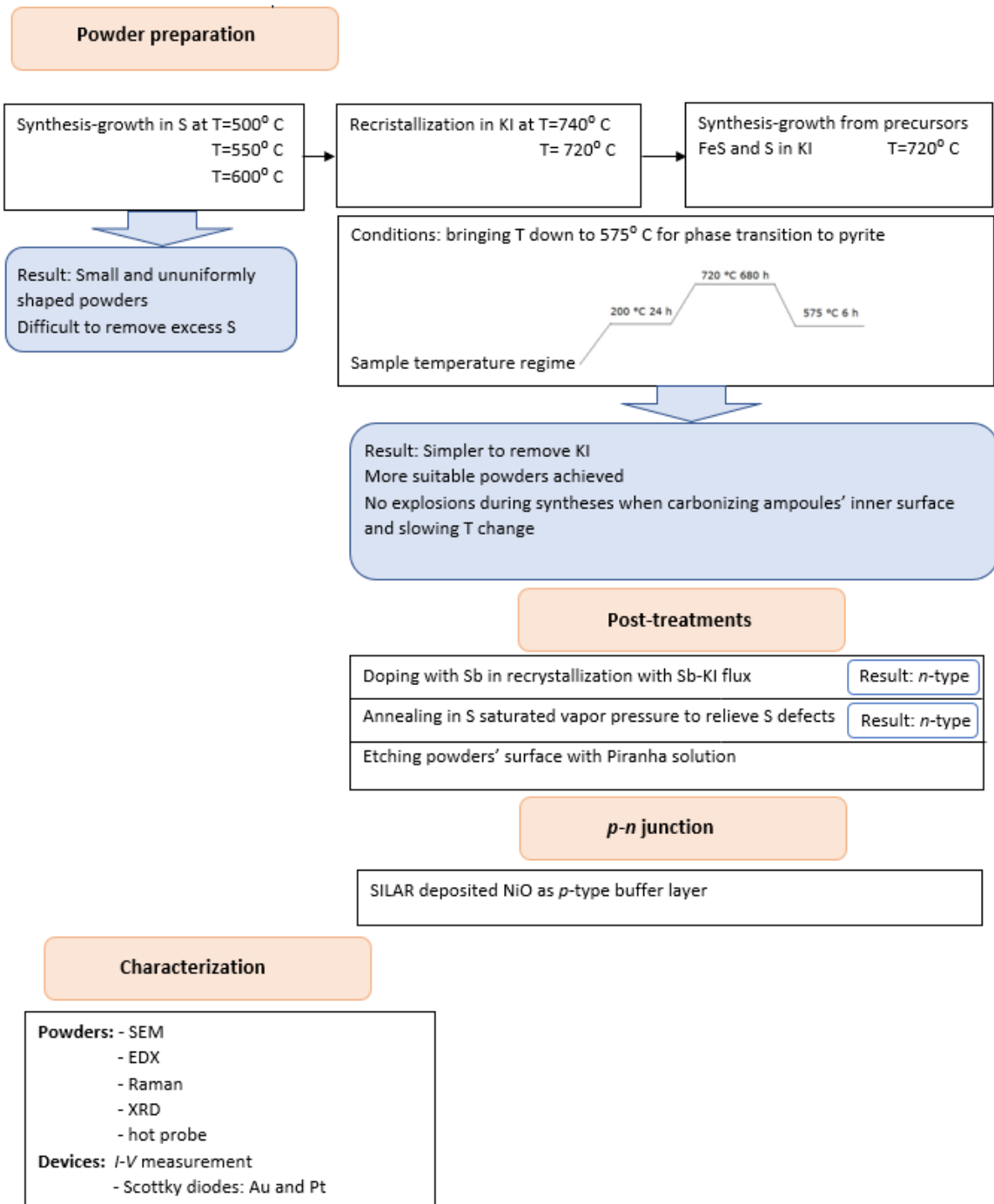- Scottky diodes: Au and Pt

Figure 2.1. Scheme of the experimental steps in the frame of FeS_2 monograin powder synthesis-growth and FeS_2 device preparation and characterization

2.1 Preparation of monograin powders

2.1.1 Using sulphur as flux

In the first experiment, all precursors FeS and S (Alpha Aesar 5N purity) were weighted in proportions needed for stoichiometric composition of pyrite. Amount of S for synthesis was weighted considering that a part of it is consumed in the reaction to form FeS_2 and another part for formation of liquid phase (flux). The mass proportions were calculated according to the needful requirement $V_{liquid}=V_{solid}$ [42]. Once added in the ampoules, the samples were degassed under dynamic vacuum while being heated to approximately 80 ⁰C. The mixtures were then sealed and heated in furnace at 500, 550 and 600 °C. The synthesis extended for one week at temperatures as stated before. After that, the process was stopped by quenching the ampoules in water. S was removed from samples by sublimation in vacuum at 125 °C. Afterwards, the powder grains were released from the remains of sulphur by leaching with KCN water solution. The washing solution with KCN did not become clear after several washing cycles. It became obvious that the FeS_2 powders being washed were dissolving in the KCN containing washing solution, because the amount of powders was decreasing visibly. Finally, the powders were washed with DI water and dried in a thermostat at 55 ⁰C.

2.1.2 Recrystallization of FeS₂ in KI flux

As the FeS_2 crystals released from S were too small for preparation of monograin membranes, the crystals synthesized in S-flux at 600 ⁰C were recrystallized in KI flux at 740 °C for one week to produce bigger grains. The temperature of the furnace was lowered from 740 to 575 °C slowly to ensure the phase transition of FeS_2 from pyrrhotite to pyrite. The furnace was kept at 575 °C for 24 hours, after that the ampoule was rapidly cooled by quenching in water to freeze pyrite polymorph in the crystals. For releasing FeS_2 crystals from solid KI-flux, rinsing with deionized water in an ultrasonic bath was used. In some next attempts to grow FeS_2 powders in KI flux at high temperatures, the ampoules exploded in the furnace during cooling. It was suspected that Fe^{2+} ions from the precursor diffused into the ampoule's SiO_2 quartz lattice and caused lattice distortion. It has been recognized [47] that the diffusion of metal cations in silica at elevated temperature produces hollow framed silica with interior voids. Diffusion of Fe cations causes polyhedral distortion and the alteration of Si−O−Si bonding in quartz. The diffusion is encouraged by the increase of annealing temperature and slow heating process (2.5 °C/min). Alloying of silica with Fe cations contributes to the

formation of metallic Si and alters quartz's physical properties, possibly including thermal coefficient. The braking of ampoules could be avoided if the inside surfaces of quartz ampoules were covered by a carbon layer. That might have inhibited Fe ion diffusion into quartz.

Once the recrystallization of FeS_2 crystals in KI, that were pre-synthesized in S, proved to be reliable, next experiments were don. It was determined whether it could be possible to synthesize and recrystallize FeS_2 in KI from precursors FeS and S straightly, in one run, without intermediate reaction of precursors to form pyrite. For that reason, two comparative experiments were made. In the first experiment, pre-synthesized FeS_2 was used. FeS_2 was obtained from heating FeS and S in stoichiometric proportion in an evacuated ampoule at 575 °C for several hours. KI was added as flux to the product FeS_2 of this synthesis. Second experiment was compiled by adding calculated amounts of FeS and S precursors mixed with KI salt straightly into one ampoule. Both ampoules were degassed and sealed. The heating process included heating at 720 °C for one week. Then the temperature was brought down slowly to 575 °C (into the pyrite region), after which the ampoules were quenched in water. Ampoules after reaction and cooling are seen in Figure 2.2.a. Solid KI was washed away with DI water agitating the dissolution in an ultrasonic bath (Figure 2.2.b). The powders were dried in a thermostat at 55 °C and sieved into narrow granulometric fractions between 38 to 112 µm.
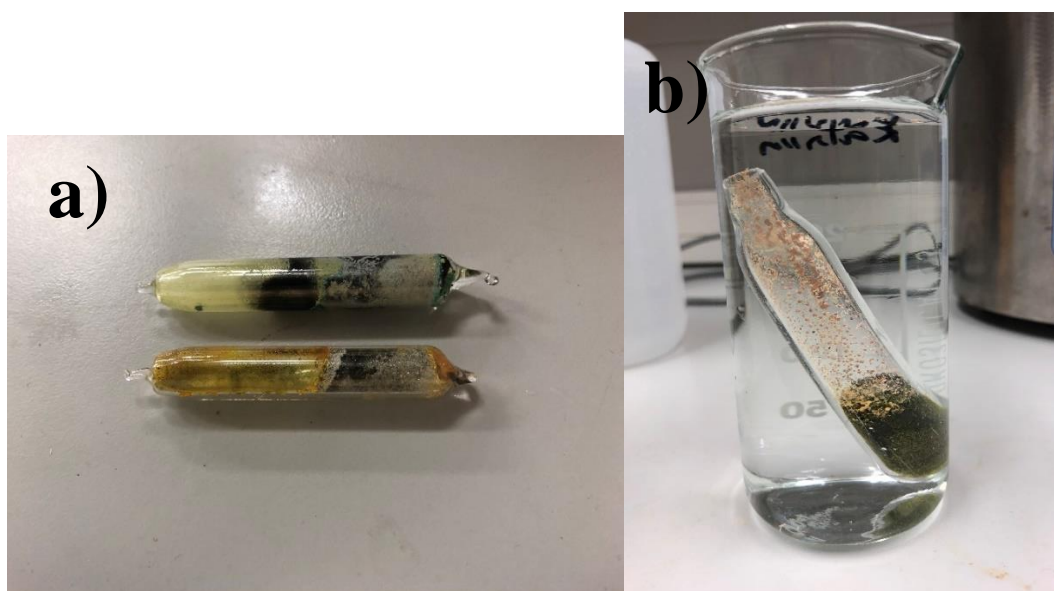

Figure 2.2.a Unopened quartz ampoules of FeS_2 – KI mixture after reaction and growth process in the furnace at high temperature. Figure 2.2.b. Opened reaction ampoule being rinsed from KI flux in DI water. Yellow color on the inside wall of ampoule is caused due to the condensed sulphur after cooling

2.1.3 Doping of FeS$_2$ with Sb in the recrystallization of FeS$_2$ in KI

Hot probe tests of the pyrite powder crystals indicated an *n*-type conductivity. Because MGL solar cells so far preferably employ a *p*-type absorber layer and *n*-type buffer layer, it was attempted to dope the pyrite crystals with antimony (Alpha Aesar 5N purity). To assure the uniform doping of all crystals, elemental powdery Sb was added to solid KI and the mixture was heated in a sealed ampoule at temperature higher than the melting temperature of KI (T_m = 680 ºC [48]) to homogenize the Sb-KI liquid mixture to be used as a doping solution in FeS$_2$ monograin recrystallization. The solidified Sb-KI mixture was then removed from the ampoule and used as flux in recrystallization of previously prepared pyrite powders. The KI-Sb dopant mixture with determined Sb concentration was distributed homogeneously into FeS$_2$ crystals and loaded into ampoules. The samples were degassed, sealed, and heated at 700 ºC for 10 h, then at 575 ºC for 50 h. After that the ampoules were quenched in water for cooling. The amount of Sb in KI was calculated so that the appropriate flux added to pyrite powders would provide 10^{20} atoms of Sb in 1 cm^3 of FeS$_2$, while full diffusion of Sb atoms into the pyrite crystal lattice was expected to occur at this elevated temperature. This was a preliminary test to dope with maximum content of Sb to verify if this technique of doping would have an effect on pyrite powders' conductivity type before designing a full series of doping experiments in a large region of concentrations from 10^{16} to 10^{20} at. cm^{-3}.

2.1.4 Annealing in sulphur vapor atmosphere

S vacancies (V$_S$) may emerge on pyrite powder crystals' surfaces during growth in KI, cooling, or washing in DI water. Therefore, the powders were post-annealed in sulphur vapor in order to relieve V$_S$ defects of both, as-grown and Sb-doped pyrite monograins. For that, two-chamber ampoules were used, where pyrite was loaded in one end and solid sulphur piece was in the other end (Figure 2.3). Two separate ampoules were used, one with as-grown pyrite powders and the other with Sb-doped pyrite crystals. The ampoules were sealed and heat-treated at 610 ºC for 10 minutes. After that the ampoules were quenched in water by cooling the sulphur side of ampoule first. This was important because when sulphur-side end of the ampoule cools first, the sulphur vapors will condense on the colder, empty side of the ampoule and not on the surface of monograins. That way the powders can be left clean from condensed sulphur.
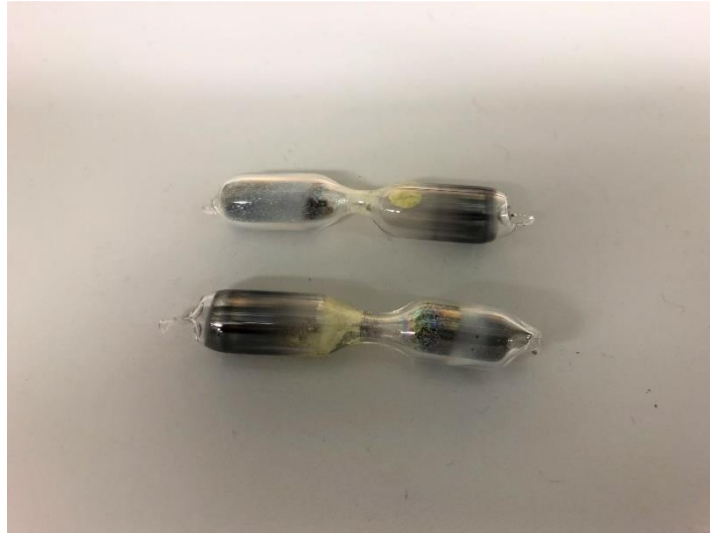
Figure 2.3. Ampoules with two chambers, separated by a narrow neck for sulphur vapor movement. One end of ampoule hosts pyrite powder crystals, the other chamber is for sulphur source. Yellow color inside the ampoule wall is the condensed sulphur after annealing and cooling

2.1.5 FeS$_2$ powder crystals' surface treatment with "Piranha solution"

To passivate the surfaces of FeS$_2$ grains and remove some surface defects, some of pyrite powders and membranes (FeS$_2$ monograins embedded in an epoxy layer) were treated in "Piranha solution" as was done in [31]. "Piranha solution" is an unofficial term that refers to a chemical etching solution, that includes 3 volume parts of concentrated H$_2$SO$_4$ and 1 part of 30% H$_2$O$_2$ solution. FeS$_2$ monograin membranes were etched in "Piranha" for 10 seconds and washed several times with distilled water with a caution not to harm the epoxy layer (epoxy can be dissolved by concentrated H$_2$SO$_4$). Powders were etched for 1 minute in "Piranha" and washed with distilled water before assembling membranes.

2.1.6 Preparation of Schottky diodes

Schottky diodes were prepared to try and assess the electrical properties of pyrite monograin layer. First, the monograin membranes were prepared by embedding the pyrite powders in epoxy. After the hardening of epoxy, metals (Au and Pt) were deposited onto FeS$_2$ monograin membranes to assemble the Schottky diodes. Metals

were chosen according to their work function, which must be higher, in case of *n*-type material, than that of the semiconductor to attain a rectifying junction [49]. If the work function of metal is lower than semiconductor's one, an Ohmic junction is developed. Work function of pyrite at room temperature is noted to be ϕ = 5.1 eV [50] while work function of gold and platinum are in between ϕ = 5.1-5.45 eV and ϕ = 5.7-6.35 eV, respectively [51], [52]. However, the materials' work functions can depend on the deposition method. Gold was deposited by thermal evaporation on as-grown pyrite membranes (Figure 2.4.a); platinum was deposited by sputtering first on a "Piranha" etched membrane (etching time 10 s), then on a membrane made of "Piranha" etched (etching time 60 s) crystals (Figure 2.4.b). Graphite and silver contacts were placed on the diode to measure *I-V* curves.
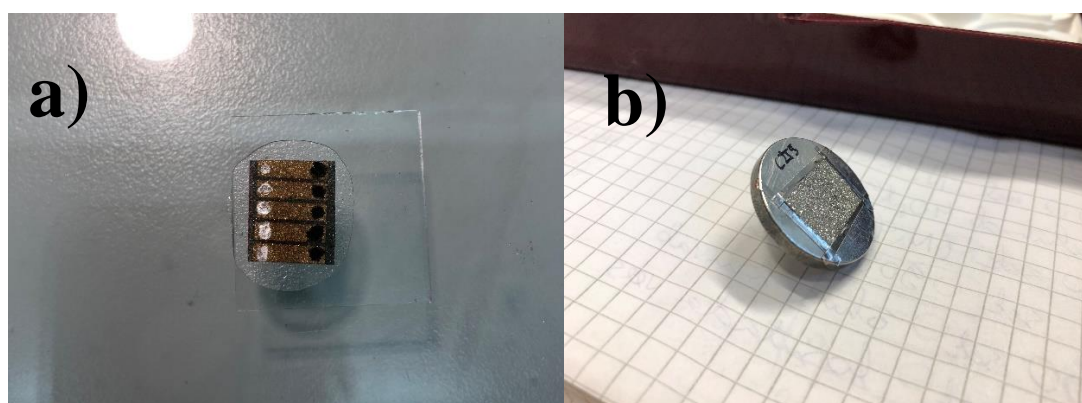

Figure 2.4.a. Schottky diode made of FeS_2 pyrite MGL and Au layer, glued on glass substrate.
Figure 2.4.b. Schottky diode made of FeS_2 pyrite MGL and Pt layer, fastened on a sample holder

2.1.7 Deposition of *p*-type buffer layer and finishing MGL solar cell

It is common for MGL solar cells to utilize a solution deposited buffer layer [38], [42], because it could be detrimental for organic polymer based monograin layers to be heated under thermal evaporation or some other high-temperature technique. High temperature could damage the epoxy that fixes monograins in the MGL (see Fig. 1.9 in the part 1.2.3). NiO was chosen as an option for the buffer layer, as it is a common *p*-type semiconductor material, has a wide bandgap and utilizes abundant nontoxic elements. NiO buffer layer was deposited by the successive ionic layer adsorption and reaction (SILAR) method. Different SILAR deposition versions were experimented in the scope of this study. First recipe proposed by Akaltun et al. [53] utilized a 0.1 M $NiSO_4$ solution. Ni^{2+} in this solution was brought to a complex with NH^{4+} ions, keeping the molar ratio 1:10 for concentration ratio of Ni:NH^{4+}. Sample was dipped

consecutively in the room temperature (RT) Ni solution and hot (90 °C) water for O^{2-} to replace NH^{4+} group. After hot water, the sample was dried and rinsed in RT water, ending one cycle of SILAR (setup on Figure 2.5). 20, 40 and 60 cycles were used for depositing films of different thickness. The deposited films were all relatively thick (50 to 150 nm) and widely cracked, therefore the Ni solution was diluted, and more experiments were conducted with a 0.02 M $NiSO_4$ solution as Ni source. The diluted solution slowed the layer deposition process and slower kinetics left time for more uniform layer growth. Deposition series with a hot Ni solution (85 °C) was experimented as well, but these results did not exhibit significant difference from the cold RT deposition. After depositing the buffer layer, the FeS_2/NiO MGL was covered by sputtering with a ZnO window layer (TCO), consisting of i-ZnO/ZnO:Al bilayer,   and finished with metal contacts on both sides.
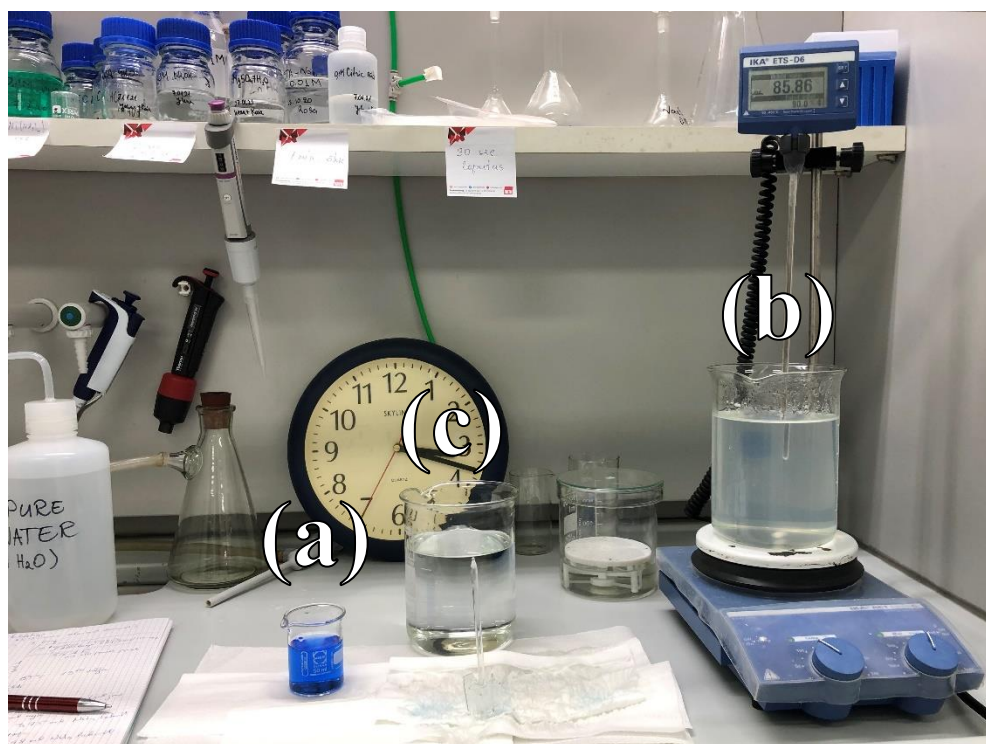

Figure 2.5. Setup of the NiO SILAR deposition. One cycle includes dipping in $[Ni(NH_3)_6]^{2+}$ solution (a), hot 90 °C water (b), drying in air, and rinsing in RT water (c)

2.2 Characterization of monograins and diodes

2.2.1 Scanning electron microscopy (SEM)

Scanning electron microscopy is one of the most versatile methods available for analysis of shape and surface morphology of different materials on a nanometer-to-micrometer scale [53]. The specimen in SEM is bombarded with a finely focused electron beam, which is scanned across the surface of the sample to return signals. The induced signals are detected and precisely amplified. Morphology of synthesized powder crystals' surfaces and bulk were studied by high-resolution scanning electron microscope (HR-SEM) Zeiss ULTRA 55.

2.2.2 Energy dispersive X-ray spectroscopy (EDX)

Energy dispersive X-ray spectroscopy was used to determine the elemental composition of synthesized powders. EDX (or XEDX) can provide information on the chemical composition of a sample for elements with atomic number higher than $Z=5$ [54]. An electron beam with energy of 10–20 keV strikes the conducting sample's surface, causing X-rays to emit from the material into the detector. In the present study the composition of materials was determined by EDX method using a Röntec EDX X-flash 3001 detector and the ZEISS HR SEM ULTRA 55.

2.2.3 Raman spectroscopy

Raman spectroscopy is a non-invasive technique used to observe vibrational, rotational, and other low-frequency modes in a system [54]. If the energy of an incident photon corresponds to the energy gap between the ground state of a molecule and an excited state, the photon may be absorbed, and the molecule promoted to the higher energy excited state. Another photon may be scattered from the affected molecule. The main scattering technique used for molecular identification is Raman scattering [54].
In this study, the phase composition of the powders was studied by room-temperature micro-Raman spectroscopy using Horiba's LabRam HR 800 spectrometer equipped with a multichannel CCD detection system. The measurement error in Raman peak position is 0,5 cm^{-1}.

2.2.4 X-ray diffraction analysis (XRD)

The crystalline structure of monograin powders was characterized by X-ray diffraction using a Rigaku Ultima IV diffractometer with monochromatic Cu Kα radiation λ = 1,54056 Å at 40 kV and 40 mA, using a D/teX Ultra silicon strip detector. For measurement, powders were grinded finely and deposited on an adhesive tape for

precise analysis. For the identification of crystal phases, the Joint Committee on Powder Diffraction Standards (JCPDS) database was used. PDXL 2 software was used for the derivation of crystal structure information from the recorded XRD data. [53]

2.2.5 Sieving analysis

The particle size distribution was determined by sieving the synthesized powder materials into narrow granulometric fractions between 38 µm to 125 µm. The sieves used separated the following fractions: 38-45, 45-56, 56-63, 63-75, 75-80, 80-90, 90-100, 100-112 and 112-125 µm. The sieving was performed on a dedicated vibrating machine or manually. The amount of material on one sieve was weighed with accuracy of 0.001 g.

2.2.6 Hot-probe experiment

A conventional hot-probe experiment enables a simple and effective way to distinguish between n-type and p-type semiconductors. In principle, a cold probe and a hot probe are connected to the semiconductor surface. The thermally excited free charged carriers move by diffusion from the hot probe to the cold probe. These majority carriers define the electrical potential sign in the multimeter. While applying the probes to an n-type semiconductor, positive voltage readout is collected in the meter, while for a p-type semiconductor, negative voltage is collected. [55]

2.3 Diode and solar cell characteristics

2.3.1 Current-voltage measurements

I-V curves were measured to evaluate the main electrical characteristics of our devices. Front and back contacts of the devices were connected to the terminals of the I-V meter and voltage was applied in forward and then reverse directions, while current was measured.

By sweeping the voltage and measuring current, it is possible to determine the creation of a rectifying junction across the device, shape of the I-V curve is determined by the transport of charge carriers through the rectifying barrier region. Measuring the diode enables to determine the built-in potential V_0, this is given by the difference in work functions of metal and semiconductor.

$$V_0 = \phi_m - \phi_{semi} \qquad (2.1),$$

where V_0 is the built-in potential, ϕ_m is the work function of the metal and ϕ_{semi} is the work function of the semiconductor material [56].

The V_0 can be read from the current-voltage graphs at the "knee point" where diode starts conducting electricity (Figure 2.6). When the diode is forward biased, a forward or positive current pass through the diode and operates in the top right quadrant of its *I-V* graph as shown in Figure 2.6. Starting at the zero intersection, the curve increases gradually into the forward quadrant, but the reverse current and voltage are extremely small. Likewise, when the diode is reversed biased, the diode blocks current except for an extremely small leakage current and operates in the lower left quadrant of its *I-V* characteristic curves. The diode continues to block current flow through it until the reverse voltage across the diode becomes greater than its breakdown voltage point resulting in a sudden increase in reverse current producing a fairly straight line downward curve as the voltage losses control (Figure 2.6).
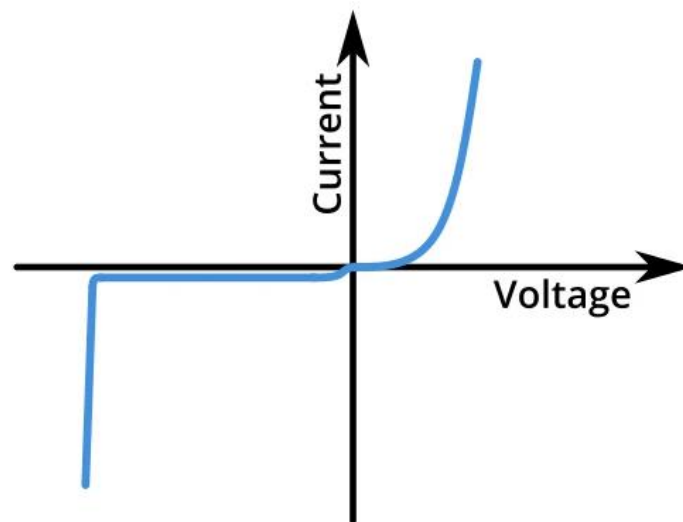

Figure 2.6. *I-V* curve of a diode [56]

2.3.2 Total transmittance and reflectance

The total transmittance and reflectance spectra of the NiO films were recorded using a Cary 5000 UV-Vis-NIR spectrophotometer (Agilent Technologies, Inc.) recorded in the wavelength range of 200– 450 nm at room temperature. Transmittance and reflectance studies enable to determine optical absorption coefficient of the material, as well as determine the optical band gap.

2.3.3 Capacitance-voltage measurements

In order to determine the carrier density of pyrite in pyrite devices, solar cells and diodes were subjected to capacitance-voltage measurements. Capacitance–voltage profiling (or $C–V$ profiling) is a technique for characterizing semiconductor materials and devices [57]. Upon applying alternating (AC) voltage to the device, test measures AC impedance, AC current, AC voltage, and impedance phase angle. Capacitance is calculated and plotted as a function of voltage. By varying the voltage applied to the junction it is possible to vary the depletion width and derive information on the semiconductor's internal characteristics, such as the carrier density, material doping profile and electrically active defect densities. Measurements in this study were done using Wayne Kerr 6500B potentiostat at different frequencies between 0.01 MHz to 10 MHz.

Table 2.1 presents which specialists in the laboratory have assisted the experiments and measurements in the scope of this study.

Table 2.1. Characterization methods used in this study

Properties	Analytical method	Specialist
Morphology	Scanning electron microscopy (SEM)	Valdek Mikli, Katriin Kristmann
Elemental composition	Energy dispersive x-ray spectroscopy (EDX)	Valdek Mikli, Katriin Kristmann
Phase composition	Raman spectroscopy	Taavi Raadik, Katriin Kristmann
Crystal structure	X-Ray Diffraction (XRD)	Erki Kärber, Katriin Kristmann
Crystals size distribution	Sieving analysis	Katriin Kristmann
Crystals electrical conductivity	Hot probe experiment	Taavi Raadik, Katriin Kristmann
Membrane preparation	Monograin membrane preparation	Maris Pilvet
Device preparation	Metal (Au and Pt) layer deposition for diodes	Maris Pilvet, Valdek Mikli
Junction formation	Current-voltage measurements	Maris Pilvet, Katriin Kristmann, Mare Altosaar
Optical properties	Transmittance and reflectance spectra	Olga Volobujeva, Taavi Raadik
Carrier density	Capacitance-voltage measurements	Taavi Raadik

3 RESULTS AND DISCUSSION

3.1 Morphology and size distribution of FeS_2 powders

The surface morphology and shape of FeS_2 crystals grown in different fluxes are presented as SEM images in Figure 3.1 – Figure 3.3. It can be seen in the figures that the crystals synthesized in sulphur as flux and post-annealed in vacuum for sulphur sublimation are not formed yet as single crystals, they consist of small particles that are sintered together, with non-homogeneous surfaces. Powders synthesized at 500 ºC (Figure 3.1) show mostly the similar morphology, while the microcrystals synthesized at 550 °C (Figure 3.2) have smoother surfaces, although some big conglomerates sintered together from smaller crystals can be seen. The average size of individual crystallites is around 1 μm. The crystal synthesis-growth preformed at 600 °C (Figure 3.3), resulted in a powder were no big differences in size and morphology could not be detected if to compare crystals from syntheses made at 550 °C and 600 °C. To assess the crystals' bulk properties, crystals were embedded in epoxy and polished to reach their cross-section. A cross-sectional SEM image of powder crystals grown in S at 500 ºC is seen in Figure 3.1. The powders are not thoroughly recrystallized and have remained porous in the middle.
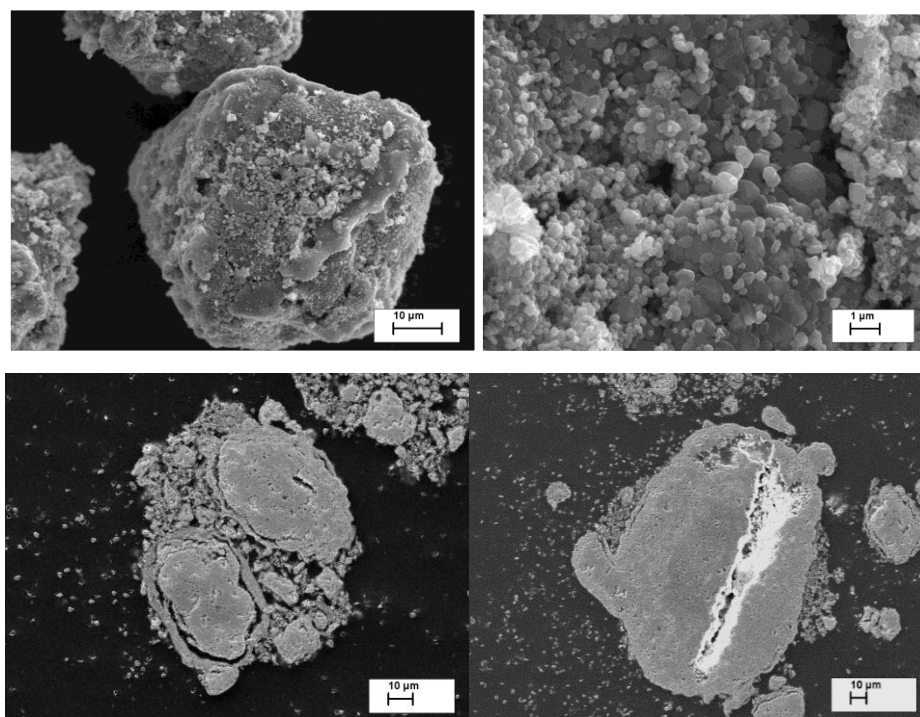

Figure 3.1. SEM images of FeS_2 particles (up left) and crystals' surfaces (up right) grown in S as flux at 500 °C. Crystals' polished cross-sectional view (bottom)
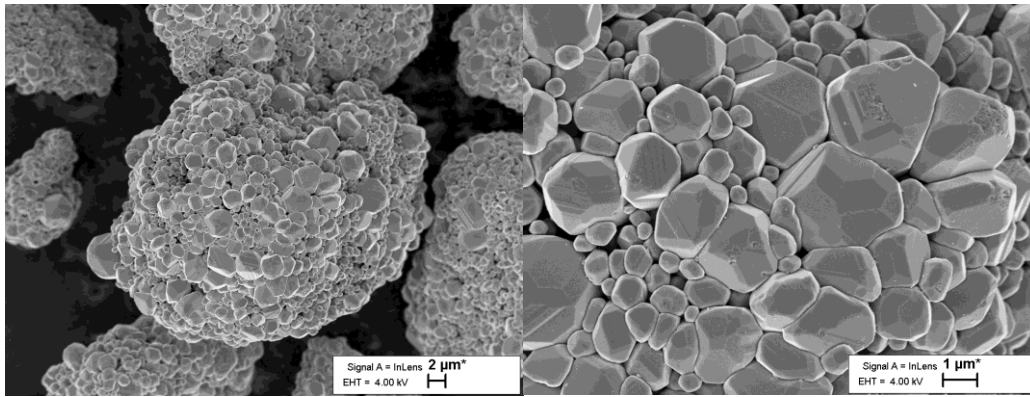
Figure 3.2. SEM images of FeS$_2$ crystals synthesized at 550 °C in S flux
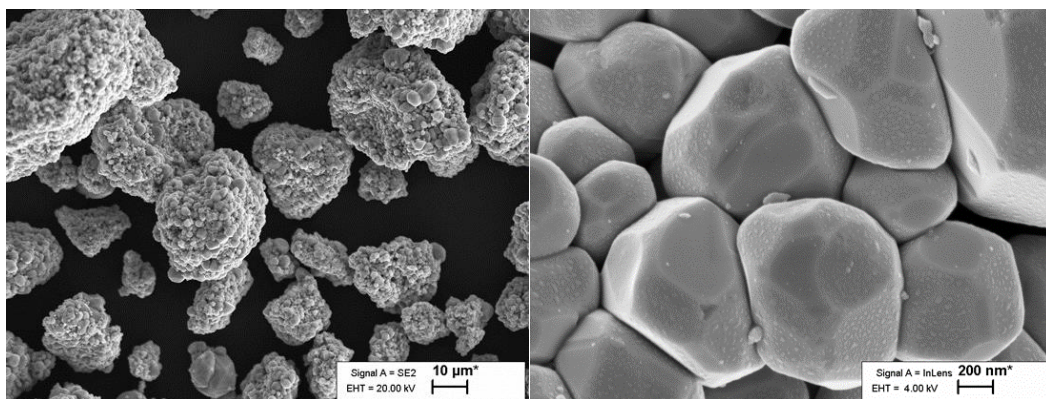

Figure 3.3. SEM images of FeS$_2$ grains synthesized at 600 °C in S flux

As the synthesis-growth in S did not result in crystals usable for monograin membrane preparation, the FeS$_2$ powder synthesized in liquid sulphur at 600 °C (see previous paragraph) were recrystallized in KI as flux at 740 °C for one week. Formed crystals had a nice uniform shape and smooth surfaces (see Figure 3.4). Roughly half of the gained powder material was in the desired fraction size of around 50 µm.
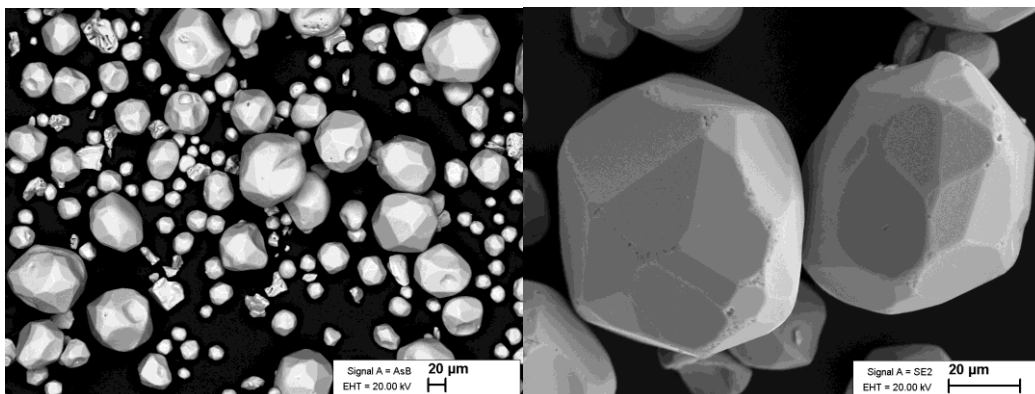

Figure 3.4. SEM images of FeS$_2$ crystals grown in KI flux at 740 °C

The following experiments to synthesize and recrystallize pyrite from precursors in KI flux yielded homogeneous round crystals with smooth surface morphology and suitable size. Figure 3.5 a,b shows crystals of FeS_2 powder, that were synthesized for the first time directly from FeS and S as separate precursors at 575 °C. Afterwards the polycrystalline powder was recrystallized in KI flux at 720 °C for one week to attain monograins. As the preliminary syntheses' tests were successful so far, in the next experiments the FeS and S precursors were loaded together with KI flux into ampoules and pyrite monograins were synthesized and recrystallized in one process. It can be seen from the micrographs in Figure 3.5 c,d that the powders' morphological quality remains high for both last cases.
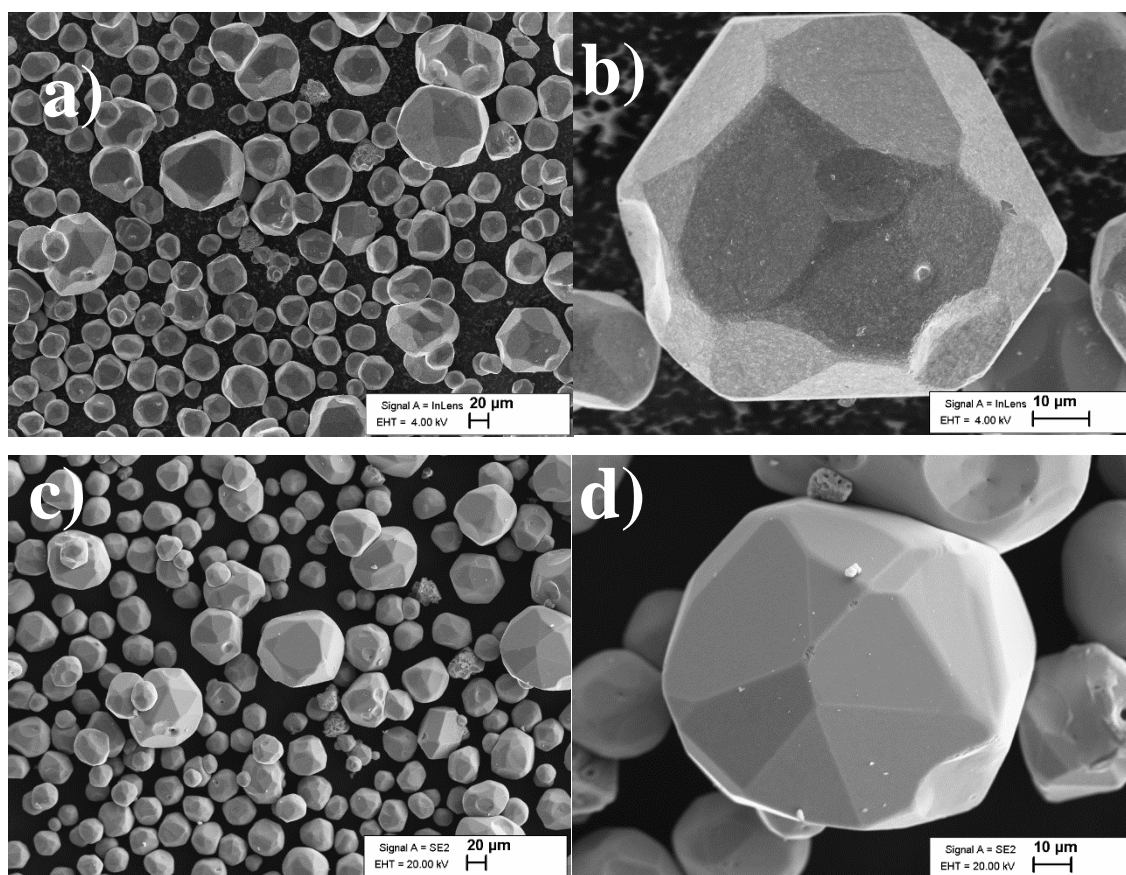

Figure 3.5. SEM images of FeS_2 crystals: a and b) pre-synthesized FeS_2 recrystallized in KI; c and d) synthesized and recrystallized in KI in one process

The small particles on the grain surface (like dust) visible on the micrographs in Figure 3.5, have the same chemical composition as the pyrite monograins. This could be explained by the phenomenon, where a part of precursors and synthesized compound dissolved in the flux at high temperatures during the process of monograin growth, precipitate onto the surface of formed crystals during cooling.

Particle size distribution analysis was used to determine the size distribution of powders synthesized in KI, the size distribution can be seen in Figure 3.6. The mass of each granulometric interval was divided by the number of µm in this interval to present the weight of different fraction sizes. The formulated graph has similarities to the normal (Gaussian) distribution predicted by the Ostwald "ripening" mechanism of crystal growth [58]. Large portion of the synthesized powders were in the suitable size fraction between 56-90 µm.
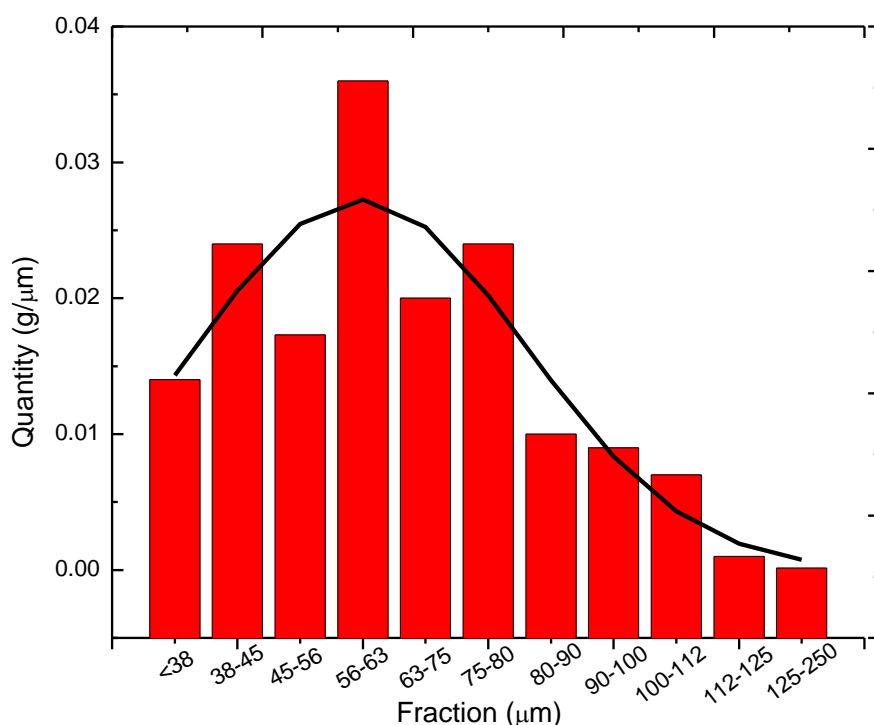

Figure 3.6. Graph of particle size distribution of powder synthesized at 720°C in KI, fitted with Gaussian distribution

3.2 Comparison of diffusion dynamics in sulphur and KI

Because the growth of powders was very different in the different flux media, it became useful to look for an explanation from the different flux properties at high temperatures. Monograin growth is governed by diffusion of reaction components, that have dissolved in the liquid phase. When it is easy for the precursors to dissolve and diffuse through flux, it is simple for them to re-deposit on the surfaces of larger crystals or solution

particles [58]. Vice versa, if the diffusion and mass transport is inhibited by low solubility or high viscosity of flux, then grain growth is depressed.

It has been widely accepted and noted by Steudel [59] that sulphur has a molecular and even polymeric nature in melts and gases at elevated temperatures. It is common for sulphur to form homocyclic rings of at least 6 atoms, with S_8 (8 S atoms) as the majority species at lower temperatures. Polymeric sulfur (S_∞) becomes a major component above 157 ⁰C (called the "polymerization temperature"), higher of which is the typical temperature range for our experiments. The polymer is said to consist of very large rings at temperatures below 157 ⁰C, above this temperature, very long diradicalic chains will start to occur. The mean chain-length of the polymer in liquid sulfur has been estimated as 10^3 atoms near 550 ⁰C. In the polymerization, where long chains form, free radicals form by homolytic S-S bond dissociation because of thermal ring opening. The radicals can also be described as dangling bonds at the chain-ends. Evidently, the radicals move rapidly around in the liquid and novel chain-like and cyclic molecules are constantly formed and destroyed [59]. These radicals may be eager to form interim bonds with Fe atoms, inhibiting the diffusion through the melt.

The viscosity of sulphur melt is influenced by the composition of molecular sulphur. At the boiling point at 446 ⁰C, viscosity reaches 0.1 Pa*s from a high point of 93.2 Pa*s at 187 ⁰C. From the boiling point, the viscosity is expected to slowly decrease with increasing temperature, as per the typical viscosity path [59].

Viscosity of KI at 720 ⁰C that was our typical crystallization temperature, is 0.0012 Pa*s [60]which is 1000x lower than sulphur at crystallization temperature. Lower viscosity may be one of the reasons for the higher growth kinetics for pyrite powders in KI liquid phase.

In an additional note, the content of halogens is reported to have an impact on the viscosity of liquid sulfur. When we made the synthesis-growth experiments, pure sulphur was added with KI (and FeS). It may have been possible that iodine from KI dissociated and diffused into liquid sulphur. Halogen content lowers the viscosity of liquid sulphur dramatically, even in low concentrations [59]. It is generally assumed that the halogens react with liquid sulfur to form chain-like dihalopolysulfanes S_nX_2. In this way the chain-length of the polymeric sulfur molecules is reduced, and the viscosity is lowered. That may catalyze the reaction-growth process by enhancing the kinetic movement and "freedom" of sulphur atoms to react with FeS precursor to form desirable FeS_2.

3.3 Elemental composition of FeS$_2$ powders

Composition of FeS$_2$ powders synthesized in different fluxes were characterized by EDX (Table 3.1). It was evident, that powders synthesized in S flux at 500 ^{o}C were sulphur poor, while other samples exhibited compositions closer to the stoichiometric composition of FeS$_2$. This could be associated with higher synthesis temperatures that enables faster diffusion of components to homogenize the overall distribution of elements. The growth process in KI, that yielded more perfect and uniform crystals, determined by SEM, also yielded desirable elemental composition for FeS$_2$.

Table 3.1. Composition of crystals grown at different temperatures and different fluxes, determined by EDX

Sample	Fe at. %	S at. %	Fe/S
500 ^{o}C in S	39.21	60.79	0.65
550 ^{o}C in S	33.06	66.94	0.49
600 ^{o}C in S	33.42	66.58	0.50
740 ^{o}C in KI	33.71	66.29	0.51
Presynthesized FeS$_2$ 720 ^{o}C in KI	33.69	66.31	0.50
From precursors 720 ^{o}C in KI	33.81	66.19	0.51

3.4 Phase composition of FeS$_2$ powders

Raman spectroscopy was performed to determine the phase composition of all samples. Because Fe$_x$S$_y$ system can have many phases simultaneously occurring in addition to pyrite, such as pyrrhotite and marcasite, the different phases' properties may change the photovoltaic parameters significantly. Therefore, the phase composition analysis was one of the most important characterization techniques of monograins.

Characteristic to pyrite phase Raman peaks are at 343, 379 and weak peaks at 350, 430 cm^{-1} [61]. It would be meaningful to look for pure sulphur peaks as well, that might have been left unreacted or unwashed, those peaks are at 220, 246, 439 and 474 cm^{-1} [62]. Secondary phases in pyrite may include hematite (Fe$_2$O$_3$) at 216 and 219 cm^{-1}. Pyrrhotite phase may appear at peaks 254, 380, 520 cm^{-1} [63]. Marcasite phase would be characterized by Raman peaks at 322, 386 cm^{-1} [64].

Raman spectra of powders synthesized in sulphur flux at different temperatures are seen in Figures 3.7.a,b,c. A slight variation in FeS_2 Raman peak positions at 343, 379, 350 and 430 cm^{-1} can be seen in the Raman spectra of samples synthesized at 500 °C and 550 °C and post-annealed in vacuum for sulphur sublimation. The shift in Raman peaks' positions could be related with removal of sulphur from the utmost surface layer of FeS_2 crystals causing the formation of S-deficient surface layer with variable composition. The shift in Raman peak positions via the formation of solid solutions is well-known [65], [66]. On the base of Raman analysis, we were able to conclude that it might be possible to avoid the formation of secondary unwanted iron sulphide phases if to proceed at higher temperatures and provide right conditions for the phase transformation.
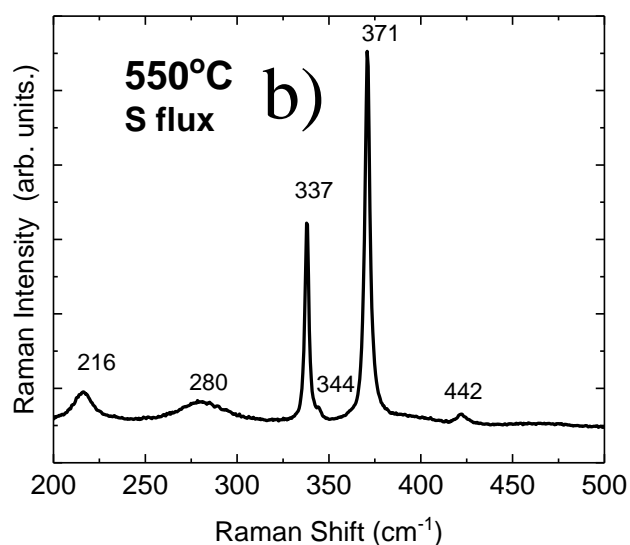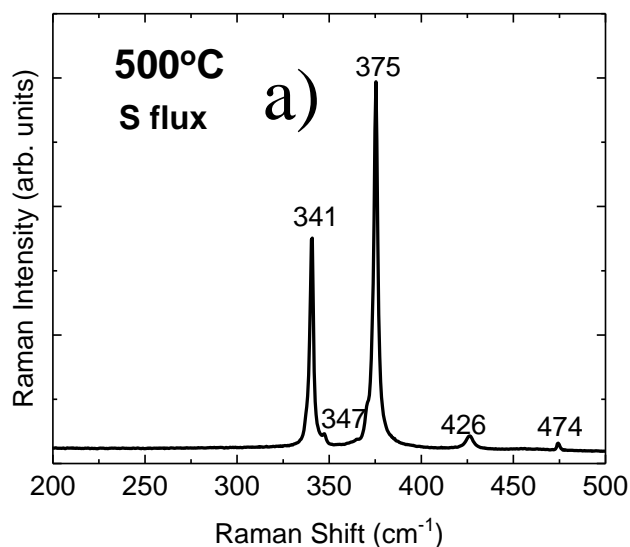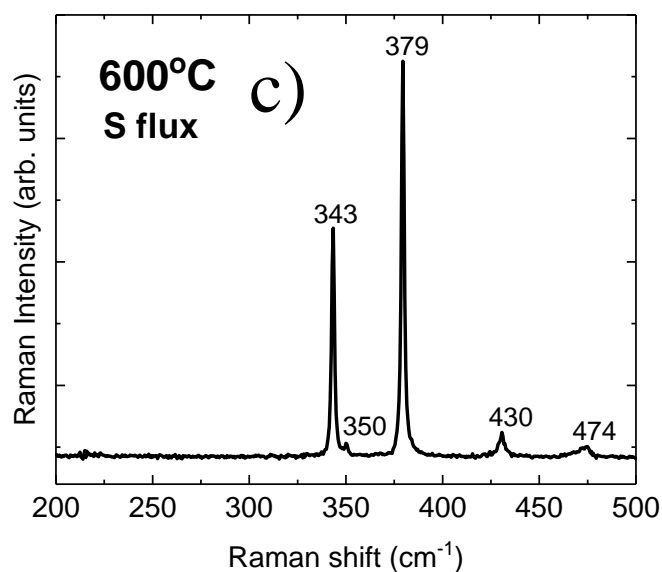
Figure 3.7. Raman spectra of pyrite powders synthesized in S flux at different temperatures a) 500⁰ C; b) 550⁰ C; c) 600⁰ C exhibiting slight shifting from pyrite peak positions 371 to 379 cm^{-1} and 337 to 343 cm^{-1}

Raman spectra of powders synthesized and crystallized in KI flux are seen in Figure 3.8. Figure (3.8.a) depicts a Raman spectrum of grains that are recrystallized in KI at 740 ⁰C from a powder previously produced at 600 ⁰C in S flux. Very sharp pyrite peaks are visible at 343, 379, and 430 cm^{-1} and a smaller one at 350 cm^{-1}. In Figure (3.8.b) there is presented a Raman spectrum of FeS_2 that was pre-synthesized separately and afterwards recrystallized in KI at 720 ⁰C. Raman spectrum of FeS_2 synthesized and recrystallized in one process in KI flux at 720 ⁰C was the same as in Figure 3.8.b. Sharp and narrow Raman signals with their peak positions characteristic to the cubic pyrite phase is proof that the grains of both materials have a high quality and no secondary phases are present. Crystallization in KI at elevated temperatures (at least 720 ⁰C) enables to gain FeS_2 monograin powders by a less complicated technological way without post-growth vacuum sublimation or etching in KCN solution as that was necessary for S flux removal.
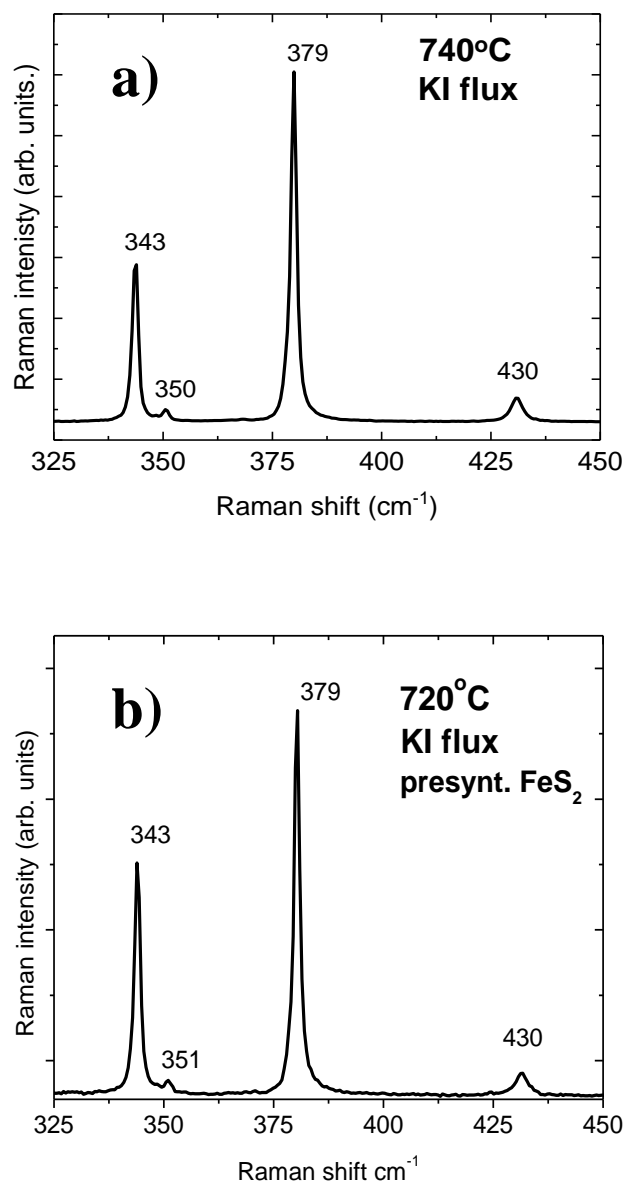
Figure 3.8. Raman spectra of pyrite powder grown in KI flux a) used material from previous experiment at 600 $^\circ$C in S flux. b) Pyrite powder from separately synthesized FeS_2 recrystallized in KI flux

All powders that were crystallized in KI were analyzed by XRD to determine the crystal structure and lattice parameter (Figure 3.9 and Figure 3.10). However, the detection of secondary phases by studying the XRD pattern may be difficult when the characteristic peaks of materials overlay with same or similar characteristic peaks of secondary phases. Additionally, if the secondary phases are in the amorphous form, it is not possible to detect them by XRD study. However, if XRD is used together with Raman spectroscopy, then it can be a useful technique for the detection of unwanted phases.

Analysis of the XRD patterns of synthesized powders gave lattice parameters $a = b = c = 5.4154$ Å. PDXL 2 software was used for the derivation of crystal structure information from the recorded XRD data (database ICDD PDF-2-2013, 00-062-0642). XRD results confirmed the cubic structure, that is in accordance with values reported in the literature [65], [66] . The XRD study supported by the Raman results show that there were no secondary phases in the crystals recrystallized in KI flux. Additionally, it was confirmed that pyrite monograins can be synthesized and recrystallized in a simultaneous process and the aforementioned experiments yield the same high-quality crystalline material. That outcome simplifies the upcoming research of the pyrite monograins significantly.
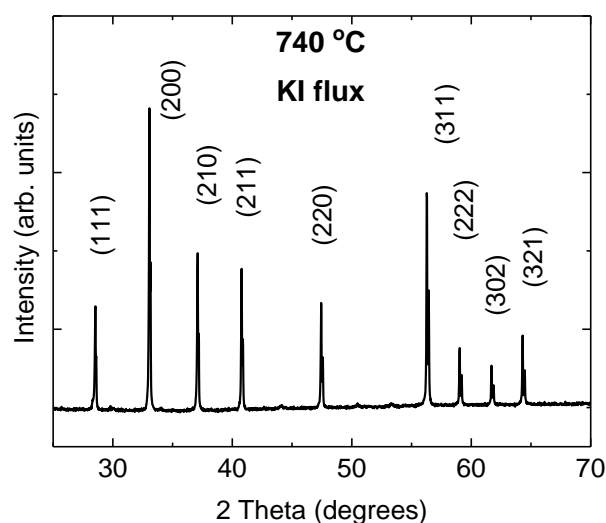

Figure 3.9. XRD pattern of crystals grown in S flux and recrystallized at 740 °C in KI flux and slowly cooled to 570 °C for phase transformation to pyrite
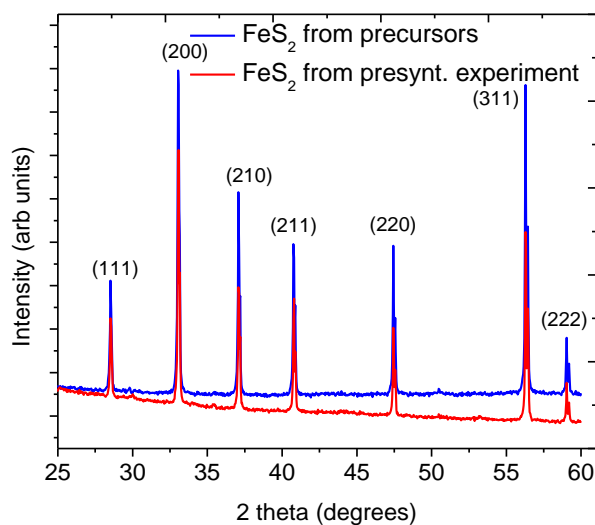

Figure 3.10. XRD pattern of crystals grown at 720 °C in KI flux from previously synthesized FeS_2 powder (red line); crystals grown at 720 °C in KI flux from FeS and S precursors (blue line)

3.5 Hot probe experiments

The hot probe measurements were conducted by placing a large (few mm) pyrite crystal between the contacts of the measurement device and heating the positive contact. Thermally excited charge carriers move from the hot contact to the cold contact by diffusion. The reading on the multimeter showed a positive value for voltage that occurred upon heating (setup on Figure 3.11). It means that the majority carriers are electrons, and it allows us to believe that the obtained pyrite crystals were *n*-type at least on the surface. Because pyrite single crystals may have a defected surface, the conductivity below the surface remains to be discovered in future studies.

Figure 3.11. Hot probe experiment with pyrite powder crystal showing *n*-type conductivity

3.6 Doping with Sb

N-type pyrite powder crystals that had been proven by Raman and XRD to be in the suitable phase composition were recrystallized in Sb-KI solution to introduce the *p*-type dopant into pyrite lattice. After the recrystallization process, cooling and washing away of the excess dopant-salt medium, hot probe tests were applied to determine the conductivity type of pyrite crystals. The crystals remained *n*-type.

Because escaping of S from pyrite crystals surfaces was suspected, the powders were reheated in sealed ampoules in sulphur saturated vapor pressure at 610 °C for 10 minutes After heat treatment, the powders were rapidly cooled and conductivity type was measured. Again, the crystals remained *n*-type. The same procedure was conducted for undoped and untreated pyrite powder crystals and the same result was achieved.

These preliminary tests lead us to focus our following attention not on trying to get the pyrite powders into *p*-type, but to focus on the achieved powders with suitable phase and morphology. To assess the *n*-type electrical properties and suitability of use, diodes were assembled, and *I-V* curves were measured, as will be explained in the following chapter.

3.7 Schottky diode experiments

Diodes were assembled and measured to assess the creation of a rectifying junction and possibly built-in voltage between the metal and an *n*-type semiconductor. Gold layer was deposited by thermal evaporation on epoxy-pyrite membrane and *I-V* curves were measured. The obtained junction proved to be nearly Ohmic by observation of the linear rise of current with linear voltage sweep (Figure 3.12).

Another type of diodes were pyrite-Pt diodes, where platinum was sputtered on top of pyrite membranes. Two types of membranes were used, one made with lightly etched (for 10 sec) crystals and the other made with etched crystals, where the surface of pyrite had been etched with a Piranha solution for 1 min. From the measurement of *I-V* curves it can be seen that a small rectifying junction is formed (Figure 3.12). There is a sharp increase in current in the forward bias and a small current in reverse bias. That corresponds to the fact that a Schottky junction conducts electricity only in forward bias and not in reverse. It can be concluded that the work function or pyrite crystals is lower than that of platinum (ϕ_{Pt} =5.7-6.35 eV [52]) and is possibly in accordance with the values in literature (ϕ_{pyrite} = 5.1 eV [50]). Nevertheless, determination of the built-in voltage V_0 from these graphs is not possible.
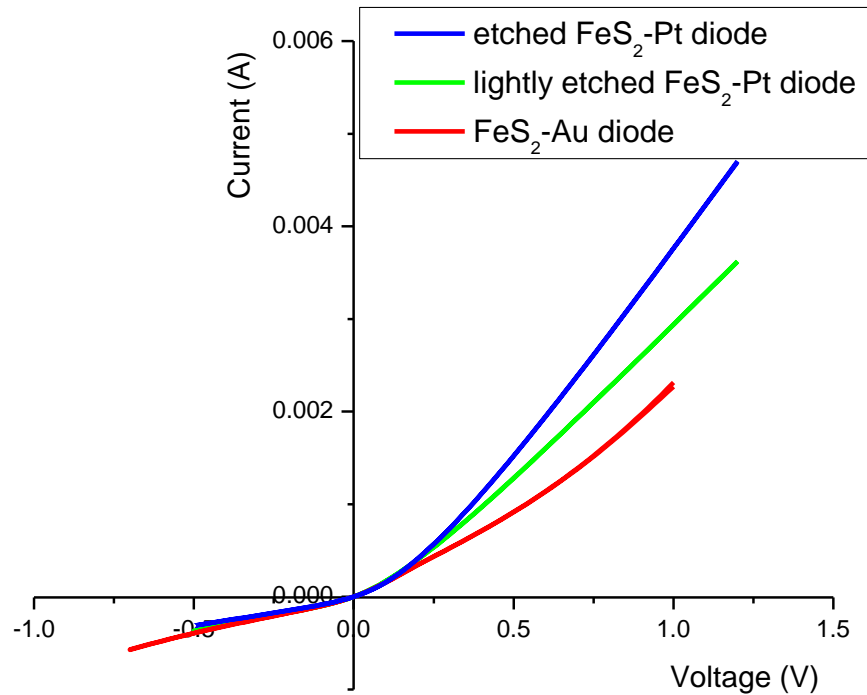
Figure 3.12. I-V curves of pyrite Schottky diodes made with Au and Pt layer

3.8 NiO buffer layer deposition and characterization

Three series of experiments were conducted to decide the proper route for *p*-type NiO buffer layer deposition by SILAR method. All series were tested on glass and on ITO slides. First series, that utilized a 0.1 M Ni solution at room temperature (RT), produced thick layers of NiO on all samples. The thickness and morphology of the samples were studied by SEM. Composition of NiO layer was determined by EDX. SEM micrographs of NiO films on glass deposited with different number of SILAR cycles (20, 40, and 60) are seen in Figure 3.13. All samples are ununiform and exhibit cracks. The quality of NiO layers decreases with the increasing number of SILAR cycles. Thickness of samples was 50 nm, 130 nm, and 150 nm, respectively. The conductivity of these films was too low for measurements by the Hall effect or van der Pauw method. In the future, NiO films should be further analyzed to determine electrical properties.
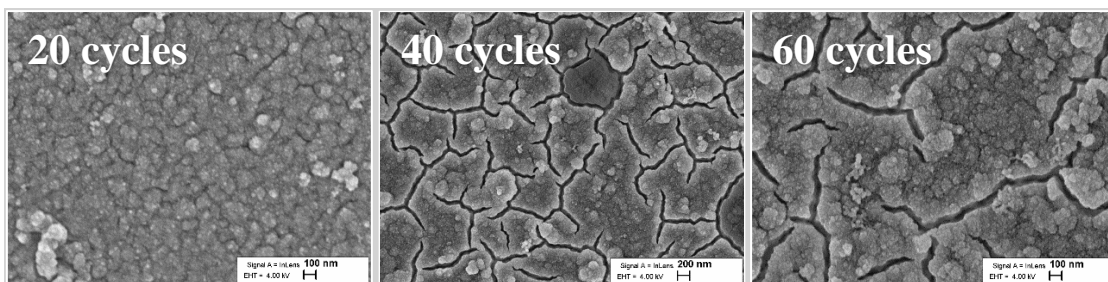
Figure 3.13. SEM micrographs of NiO layers on glass, deposited with different number of SILAR cycles – 20, 40, and 60, from left to right

Next experiments utilized a 0.02 M Ni solution to slow down the layer deposition rate and allow the formation of NiO crystals with more perfect crystallinity. Figure 3.14 shows NiO films deposited from a RT Ni solution. Both RT and hot solution NiO deposition series were performed on ITO glass and on pyrite membranes with the aim to test the NiO films' adhesive properties on ITO glass and FeS$_2$ MGLs. It can be seen in Figure 3.13 that the NiO films are more uniform and with less apparent cracks than they were on glass substrates as previously described. It was concluded that the diluted solution provided better morphological properties.
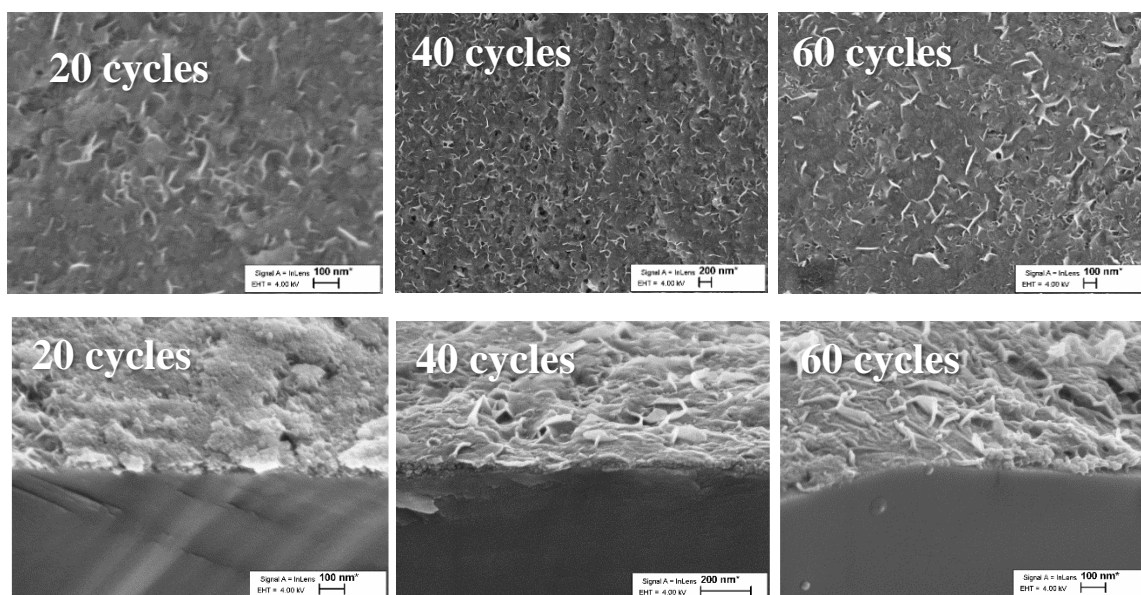

Figure 3.14. NiO films deposited on ITO glass (1st row) and on pyrite monograin membranes (2nd row). Number of SILAR cycles is 20, 40 and 60 – from left to right

NiO layers deposited from hot Ni solution were very similar to the films deposited from RT solutions. The micrographs are not presented here to avoid repetition.

3.8.1 NiO layer transmittance and band gap

The optical transmittance spectra of NiO films were recorded to assess the optical quality of NiO deposited at different temperatures and dipping cycles (Figure 3.15). Transmittances brought in Figure 3.15 depict NiO films deposited from 0.02 M NiSO$_4$ solution. Measurements were conducted in the wavelength range of 200–450 nm at room temperature. The transmittance values vary in the range of 60% to 90% in the visible spectrum without significant dependence on solution temperature or deposition cycles. Rather, it may be concluded that the deposition temperature does not play a significant role in the film transmittance.
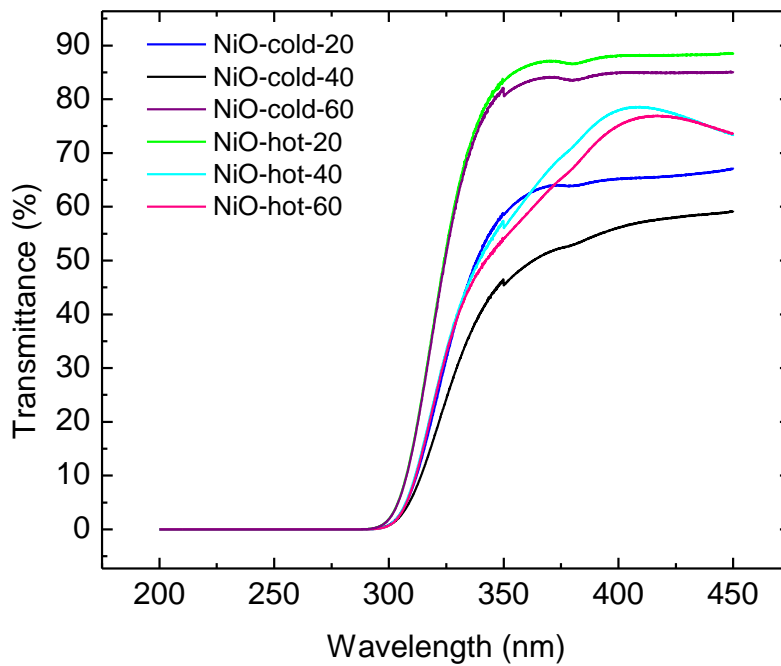

Figure 3.15. Transmittance spectra of NiO films deposited by different cycles of SILAR method from hot and cold 0.02 M NiSO$_4$ solutions. Numbers 20, 40 and 60 in line designations mark the SILAR cycles

The optical direct bandgap (E_G) of NiO was determined by extrapolation of the linear portion of the (ahv)^2 vs. hv plot (Tauc plot on Figure 3.16) to meet the x-axis. To draw a Tauc plot, the absorption coefficient, a, was calculated using equation:

$$\alpha = \frac{1}{d} ln \left(\frac{1-R}{T}\right)$$

(3.1)

where a is the absorption coefficient, d is the thickness of the film, T is the total transmittance, and R is the total reflectance.
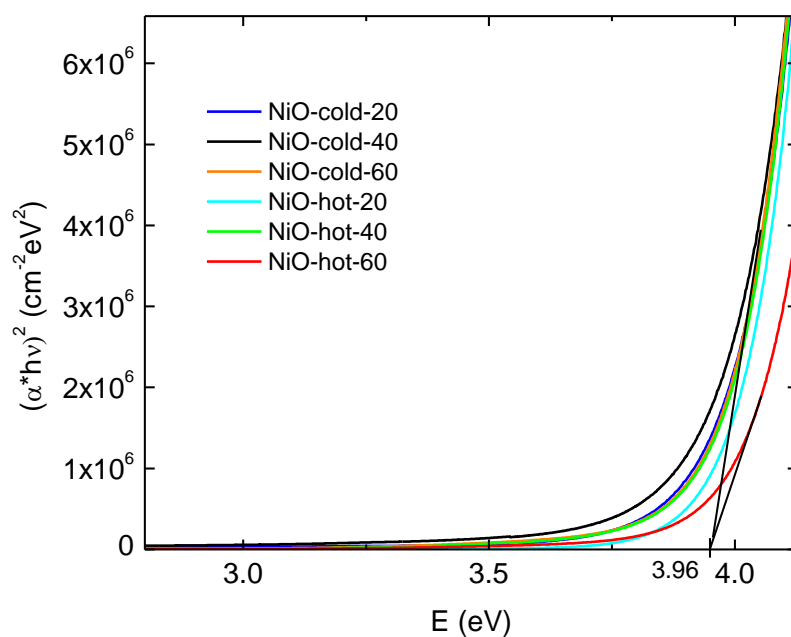
Figure 3.16. Tauc plot of NiO films deposited by SILAR method from hot and cold Ni solutions

All the samples showed very similar values of optical bandgap in the range of E_G=3.95 – 3.97 eV that can be seen in Table 3.2. That correspods with values from literature.

Table 3.2. Bandgap energies of NiO films deposited at different temperatures

Sample	Bandgap energy
NiO – cold – 20	3.96 eV
NiO – cold – 40	3.95 eV
NiO – cold – 60	3.97 eV
NiO – hot – 20	3.97 eV
NiO – hot – 40	3.96 eV
NiO – hot – 60	3.97 eV

3.9 Solar cell with NiO buffer layer

First solar cells made with pyrite powders in monograin layer technology were measured for characterizing their current-voltage characteristics. It can be seen from Figure 3.17 that a junction between pyrite and SILAR deposited (20 cycles) NiO has been formed but no photocurrent is generated in the solar cell. In the future these results may be improved by further work in pyrite monograins surface defects, doping, and experimenting with different buffer layers and device architectures.
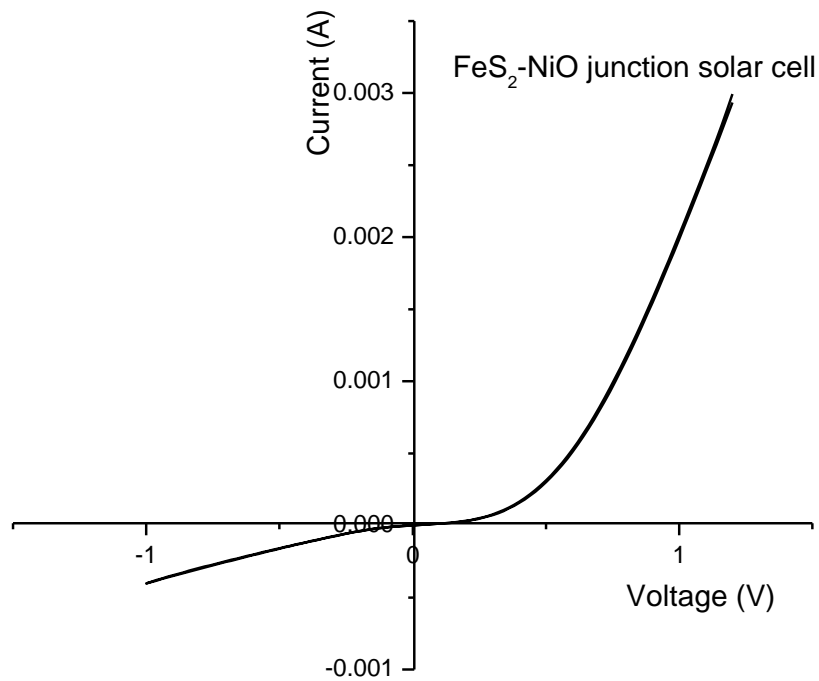
Figure 3.17. *I-V* characteristics of the first FeS_2-NiO junction solar cell

3.10 Carrier density of pyrite

Carrier density of pyrite was calculated using data from capacitance-voltage measurements. Measurements were conducted at frequencies 0.01 MHz, 0.1 MHz, 1 MHz, 10 MHz, and 10 MHz. The carrier density result depends deeply on the measurement frequency. It must be assured that the measurement frequency is lower than the modified dielectric relaxation frequency of the charge carriers. Represented in Figures 3.18a and b are Mott-Schottky plots of pyrite-Pt diode and pyrite-NiO solar cell devices measured at f = 1 MHz as this was the frequency where the most reliable results were obtained. For depicting a Mott-Schottky plot capacitances ($1/C^2$) were calculated and plotted against voltage. Carrier density values were expressed from the following formula of capacitance:

$$C^{-2}=2(U_{bi}-U)/A^2q\varepsilon N_D \qquad\qquad (3.2)$$

where C is capacitance from measured impedance values, U_{bi} is built-in voltage or barrier difference between metal and semiconductor Fermi levels, U is applied voltage, A is area of active device, ε is material dielectric permeability, N_D is ionized donor density. Donor density is derived by fitting a trendline to the downward part of Mott-Schottky graph and calculating based on the slope. Carrier density for the pyrite-Pt Schottky diode was $2.5*10^{17}$ cm^{-3}, while carrier density for the pyrite-NiO heterojunction solar cell was $6.2*10^{16}$ cm^{-3}.
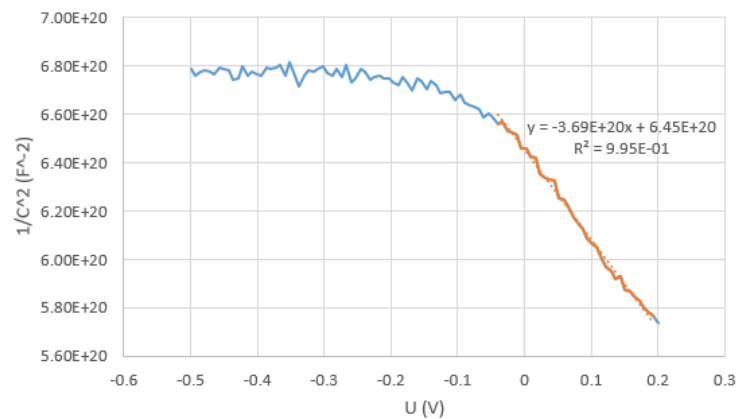

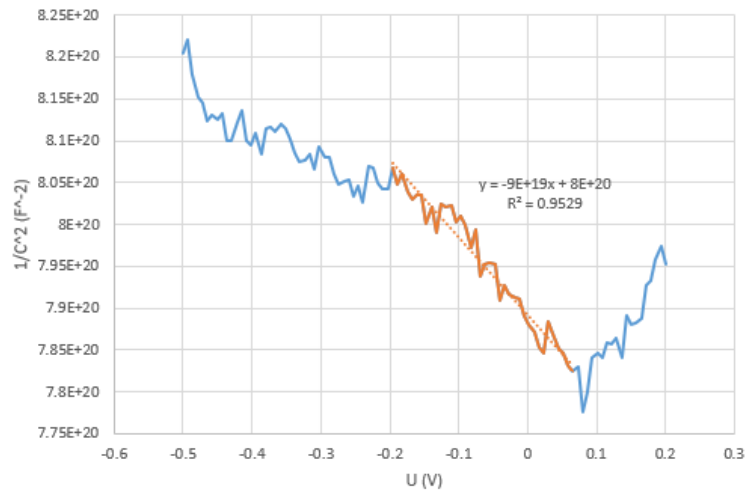Figure 3.18.a. Mott-Schottky graph ($1/C^2$ vs U) of pyrite-NiO solar cell

Figure 3.18.b. Mott-Schottky graph ($1/C^2$ vs U) of pyrite-Pt Schottky diode

SUMMARY

In this study, recrystallization and synthesis-growth of FeS_2 monograin powders were performed in the molten phase of two different flux materials (S and KI) at different temperatures - at 500^0 C, 550^0 C, 600^0 C in S and at 720^0 C/575^0 C, 740^0 C/575^0 C in KI. The cooling temperature profiles were modified to guarantee the phase transition into pyrite phase. FeS_2 as a promising solar cell absorber material was investigated for use in monograin layer solar cell for the first time. The grown monograin powder materials were characterized by SEM, XRD, Raman, EDX and by hot probe method. The powder crystals were used for making monograin membranes for solar cells. In contact with NiO and Pt the carrier concentration of FeS_2 was determined by *C-V* measurements. From the made powder analyses the next results were found:

- SEM micrographs showed that powders synthesized in S flux were not formed as single crystals, but consisted of small particles that were sintered together, with irregular (non-homogeneous) surfaces. Some crystals remained porous in the middle. These results were similar for powders synthesized at all temperatures in liquid sulphur medium. SEM micrographs of powders grown in KI flux at 720^0 C and at 740^0 C had uniform round shape and smooth surfaces.

- Average size of powder crystals grown in S flux was around 1 µm, additionally, the yield of powder was quite low. As for the powders grown in KI, a large portion of them was in the size fraction between 56-90 µm suitable for MGLs, and the yield of powders was high.

- According to the EDX, powders synthesized in S flux at 500 ^{0}C were sulphur poor, while other samples exhibited compositions closer to the stoichiometric composition of FeS_2. The growth process in KI yielded desirable stoichiometric elemental composition for FeS_2.

- Phase composition of FeS_2 powders was determined by Raman and XRD analysis. The positions of Raman peaks of pyrite were slightly shifted for powders grown in S flux, indicating possible sulphur poor secondary phases on the surface. Powders grown in KI were determined to be in the pyrite phase by both, Raman and XRD analysis.

- All powders grown in KI were of *n*-type conductivity by the hot probe method.

Schottky diodes were assembled based on pyrite monograin layer, and a rectifying junction was obtained in the FeS$_2$-Pt architecture. The rectifying effect was more obvious if the FeS$_2$ powder crystals were etched with "Piranha solution".

First solar cells from pyrite powders in monograin layer design were assembled with *p*-type NiO to measure current-voltage characteristics. Monograin solar cells with a *p*-type buffer layer had not been utilized before this study. NiO was deposited by subsequent ionic layer adsorption and reaction (SILAR) method. The pyrite-NiO device showed a formation of rectifying junction between the materials but no photocurrent was detected. These results may be improved by further work with surface treatments and doping of pyrite.

Lastly, majority carrier density of FeS$_2$ was determined from capacitance-voltage (*C-V*) measurements. *C-V* measurements were carried out on pyrite based Schottky diodes with Pt junction, and solar cells with NiO buffer layer. Carrier density of pyrite microcrystals, determined from the Schottky diode was $2.5*10^{17}$ cm^{-3}, and from the pyrite solar cell $6.2*10^{16}$ cm^{-3}, respectively.

The next conclusions can be drawn from this study:

1. It is possible to grow stoichiometric and phase pure pyrite FeS$_2$ monograin powders from precursors in KI molten phase. KI enables to produce *n-type* powder crystals with uniform round shape and smooth surfaces. Additionally, sulphur is not a suitable flux for this process for the difficulties of removing it.

2. It is shown that devices based on FeS$_2$ monograin layers with a *p*-type buffer layer (FeS$_2$/NiO) have potential for use in pyrite monograin layer solar cells.

KOKKUVÕTE

Käesolevas töös on uuritud püriitse FeS_2 monoterapulbri süntees-kasvatust kahes erinevas sulandajas (väävel ja kaaliumjodiid) erinevatel temperatuuridel - 500º C, 550º C, 600º C väävlis ning 720º C/575º C, 740º C/575º C KI-s. Jahutusrežiime muudeti vastavalt vajadusele kindlustada materjali üleminek pürrhotiitfaasist püriidi faasi. FeS_2 kui paljulubavat päikesepatarei absorbermaterjali rakendamist monoterakiht-päikesepatareis uuriti esmakordselt. Sünteesitud monoterapulbreid karakteriseeriti skanneeriva elektronmikroskoopia (SEM), röntgendifraktsiooni (XRD), Raman spektroskoopia ja energiadisperseeruva röntgenkiirgusspektroskoopia (EDX) uurimismeetoditega. FeS_2 kristalle kasutati monoteramembraanide valmistamiseks päikesepatareide jaoks. Kontaktis nikkeloksiidi ja plaatinaga leiti mahtuvus-pinge (*C-V*) mõõtmiste kaudu püriidi laengukandjate kontsentratsioon. Pulbrite analüüsimisel jõuti järgmiste tulemusteni:

• SEM-i tulemused näitasid, et pulbrid, mis olid sünteesitud sulas väävlis, ei olnud moodustanud üksikkristallidest, vaid koosnesid väikestest kokkupaakunud osakestest, millel oli ebaühtlane pinnakiht. Mõned kristallid olid seest poorsed. Need tulemused olid sarnased kõikide pulbrite puhul, mis olid väävelsulandajas sünteesitud. KI-sulandajas kasvatatud pulbrite kuju oli ühtlane, ümar ja terad olid siledate pindadega nii 720º C kui 740º C kasvatuste puhul.

• Pulbrite keskmine suurus väävel-sulandaja puhul oli umbes 1 μm, kusjuures saagis oli üsna madal. KI-s kasvatatud pulbrite puhul oli saagis suurem ja suur osa pulbrist oli 56-90 μm suurusfraktsioonis, mis on sobilik monoterakihi valmistamiseks.

• EDX-i tulemused näitasid, et väävlis 500º C juures kasvatatud pulbrid olid väävlivaesed, teistest sünteesidest saadi stöhhiomeetriale paremini vastavaid FeS_2 pulbreid. Kasvatus KI-s andis stöhhiomeetriale vastava koostisega FeS_2 pulbrid.

• FeS_2 faasikoostis määrati Ramani ja XRD metoditega. Püriidi Raman-spektri tippude asukohad nihkusid pisut väävlis kasvatatud pulbri puhul, viidates võimalike väävlivaesete faaside kohalolule püriidi pinnal. KI-s kasvatatud pulbrid olid püriidi faasis vastavalt Ramani ja XRD analüüsidele.

• Kõik KI-s kasvatatud pulbrid olid *n*-tüüpi juhtivusega, nagu määrati nn. kuuma sondi juhtivusmõõtmisega.

Schottky dioodid moodustati püriidi monoterakihtidest ja dioodi üleminek saadi FeS_2-Pt järjestuse (kontakti) juures. Üleminek oli selgem nende dioodide puhul, mille kokkupanemiseks oli kasutatud püriidi kristalle, mis olid eelnevalt söövitatud nn. Piranha lahusega.

Püriidi monoterakiht-päikesepatarei struktuur koostati *n*-tüüpi püriidi katmise teel (kontakteerimisel) *p*-tüüpi NiO kihiga *p-n* ülemineku moodustamiseks, et mõõta pinge-voolu karakteristikuid. Monoterakiht-päikesepatareide sellist struktuuri, kus *n*-tüüpi absorber ja *p*-tüüpi puhver moodustavad ülemineku, ei oldud enne seda uurimust rakendatud. NiO sadestati vesilahusest SILAR-meetodi abil (*subsequent ionic layer adsorption and reaction*). Püriit/NiO struktuuri *V-A* kõverad näitasid dioodi-laadset käitumist, kuid päikesesimulaatoriga valgustades ei näidanud voolu. Neid esmaseid tulemusi on võimalik parandada, kui süvitsi uurida püriidikristallide legeerimise ja pinnatöötluste mõju.

Püriidi laengukandjate kontsentratsioon määrati *C-V* mõõtmistega, mis viidi läbi püriidi-Pt dioodi ja püriidi-NiO päikesepatarei struktuuridel. Langukandjate kontsentratsioon oli $2.5*10^{17}$ cm^{-3} dioodi puhul ning $6.2*10^{16}$ cm^{-3} päikesepatarei puhul.

Antud töö põhjal on võimalik tuua järgmised järeldused:

1. Stöhhiomeetrilisi ja faasipuhtaid FeS_2 püriidi monoterapulbreid on võimalik sünteesida KI-sulandajas. Nii on võimalik toota *n*-tüüpi pulbreid, mille kristallide kuju on ümar, ühtlane ja sileda pinnaga. Väävel ei ole sobilik sulandaja FeS_2 monoterapulbri kasvatamiseks, kuna seda on pärast keeruline eemaldada.

2. FeS_2 monoterakihi tehnoloogial põhinevad seadmed *p*-tüüpi puhverkihiga (FeS_2/NiO) on näidanud potentsiaali kasutamaks püriiti monoterakiht-päikesepatareides.

LIST OF REFERENCES

[1]   United Nations, "Climate Change and Land Report," 2019.

[2]   M. R. Hannah Ritchie, "Renewable Energy," *Our World in Data, Retrieved from https://ourworldindata.org/renewable-energy 12.03.2021*, 2020.

[3]   European Commission, "Energy Roadmap 2050," Luxembourg, 2012.

[4]   B. Parida, S. Iniyan, and R. Goic, "A review of solar photovoltaic technologies," *Renewable and Sustainable Energy Reviews*, vol. 15, pp. 1625–1636, 2011.

[5]   V. Devabhaktuni, M. Alam, S. Shekara Sreenadh Reddy Depuru, R. C. Green, D. Nims, and C. Near, "Solar energy: Trends and enabling technologies," *Renewable and Sustainable Energy Reviews*, vol. 19. Pergamon, pp. 555–564, Mar. 01, 2013. doi: 10.1016/j.rser.2012.11.024.

[6]   C. Luan, X. Sun, and Y. Wang, "Driving forces of solar energy technology innovation and evolution," *Journal of Cleaner Production*, vol. 287, p. 125019, Mar. 2020, doi: 10.1016/j.jclepro.2020.125019.

[7]   A. ; T. H. Ennaoui, "Iron sulphide solar cells," *Solar Cells*, vol. 13, pp. 197–200, 1984.

[8]   C. Wadia, A. P. Alivisatos, and D. M. Kammen, "Materials Availability Expands the Opportunity for Large-Scale Photovoltaics Deployment," *Environmental Science & Technology*, vol. 43, no. 6, Mar. 2009, doi: 10.1021/es8019534.

[9]   L. Yu *et al.*, "Iron Chalcogenide Photovoltaic Absorbers," *Advanced Energy Materials*, vol. 1, no. 5, Oct. 2011, doi: 10.1002/aenm.201100351.

[10]   "Basic Photovoltaic principle and method," *Solar Information Module 6213*, vol. SERI/SP-290-1448, Feb. 1982.

[11]   Solenergy Systems Inc, "EDMOND BECQUEREL: THE MAN BEHIND SOLAR PANELS," *https://solenergy.com.ph/solar-panel-philippines-edmond-becquerel/ Retrieved on 1.02.2021*.

[12]   "Energy band diagram," *https://2012books.lardbucket.org/books/principles-of-general-chemistry-v1.0m/s16-06-bonding-in-metals-and-semicond.html Retrieved 1.02.2021*.

[13]   Optics for Engineers, "Abrupt PN junction at thermal equilibrium," *http://www.optique-ingenieur.org/en/courses/OPI_ang_M05_C02/co/Contenu_05.html Retrieved 1.02.2021*.

[14]   D. G. Dye, "Spectral composition and quanta-to-energy ratio of diffuse photosynthetically active radiation under diverse cloud conditions," *Journal of Geophysical Research*, vol. 109, no. D10, 2004, doi: 10.1029/2003JD004251.

[15]   J. S. Hill, "Multicrystalline Silicon Modules To Dominate Solar PV Industry," *https://city.engins.org/external/multicrystalline-silicon-modules-to-dominate-solar-pv-industry-in-2014/view/ (attained 5.02.2021)*, Nov. 2013.

[16]   AMERICAN PHYSICAL SOCIETY, "April 25, 1954: Bell Labs Demonstrates the First Practical Silicon Solar Cell," *APS Physics https://www.aps.org/publications/apsnews/200904/index.cfm (Retrieved on 13.04.2021)*, 2009.

[17]   Y. Liu *et al.*, "High-Efficiency Silicon Heterojunction Solar Cells: Materials, Devices and Applications," *Materials Science and Engineering R: Reports*, vol. 142. Elsevier Ltd, p. 100579, Oct. 01, 2020. doi: 10.1016/j.mser.2020.100579.

[18]   M. A. Green, E. D. Dunlop, J. Hohl-Ebinger, M. Yoshita, N. Kopidakis, and A. W. Y. Ho-Baillie, "Solar cell efficiency tables (Version 55)," *Progress in Photovoltaics: Research and Applications*, vol. 28, no. 1, Jan. 2020, doi: 10.1002/pip.3228.

[19]   NREL - National Renewable Energy Laboratory, "Best Research-Cell Efficiency Chart," *https://www.nrel.gov/pv/cell-efficiency.html (retrieved 20.02.2021)*, 2021.

[20]   E. Spooner, "Organic Photovoltaics vs 3rd-Generation Solar Cell Technologies," *Ossila. Enabling materials science*, 2021.

[21]   M. Rahman, G. Boschloo, A. Hagfeldt, and T. Edvinsson, "On the Mechanistic Understanding of Photovoltage Loss in Iron Pyrite Solar Cells," *Advanced Materials*, vol. 32, no. 26, Jul. 2020, doi: 10.1002/adma.201905653.

[22]   A. P. S. S. I. R. P. SRIVASTAVA, "n-TYPE IRON PYRITE (FeS2) THIN-FILMS OBTAINED AT DIFFERENT SULFUR VAPOR PRESSURES," *Chalcogenide Letters*, vol. 14, no. 6, pp. 227–237, 2017.

[23]   C. Steinhagen, T. B. Harvey, C. J. Stolle, J. Harris, and B. A. Korgel, "Pyrite Nanocrystal Solar Cells: Promising, or Fool's Gold?," *The Journal of Physical Chemistry Letters*, vol. 3, no. 17, Sep. 2012, doi: 10.1021/jz301023c.

[24]   S. Mohr, D. Giurco, M. Yellishetty, J. Ward, and G. Mudd, "Projection of Iron Ore Production," *Natural Resources Research*, vol. 24, no. 3, Sep. 2015, doi: 10.1007/s11053-014-9256-6.

[25]   M. Birkholz, "Modeling the Shape of Ions in Pyrite-Type Crystals," *Crystals*, vol. 4, no. 3, Sep. 2014, doi: 10.3390/cryst4030390.

[26]   S. W. Lehner, N. Newman, M. van Schilfgaarde, S. Bandyopadhyay, K. Savage, and P. R. Buseck, "Defect energy levels and electronic behavior of Ni-, Co-, and As-doped synthetic pyrite (FeS2)," *Journal of Applied Physics*, vol. 111, no. 8, Apr. 2012, doi: 10.1063/1.4706558.

[27]   ASM International Alloy Phase Diagram and Handbook Committees, "Alloy phase Diagrams," in *ASM Handbook Vol. 3*, Hugh Baker, Hiroaki Okamoto, and Scott D. Davidson, Eds. The Materials Information Society, 1992, pp. 243-undefined. Accessed: Feb. 05, 2021. [Online]. Available: http://behineh-sazan.ir/wp-content/uploads/2016/12/ASM.Vol-3.pdf lk 243 / 522

[28]   T. Jantzen, K. Hack, E. Yazhenskikh, and M. Müller, "Evaluation of thermodynamic data and phase equilibria in the system Ca–Cr–Cu–Fe–Mg–Mn–S part I: Binary and quasi-binary subsystems," *Calphad*, vol. 56, Mar. 2017, doi: 10.1016/j.calphad.2016.04.011.

[29]   M. Hillert and L.-I. Staffansson, "An analysis of the phase equilibria in the Fe−FeS system," *Metallurgical and Materials Transactions B*, vol. 6, no. 1, Mar. 1975, doi: 10.1007/BF02825676.

[30]   G. Manthilake *et al.*, "Thermal Conductivity of FeS and Its Implications for Mercury's Long-Sustaining Magnetic Field," *Journal of Geophysical Research: Planets*, vol. 124, no. 9, Sep. 2019, doi: 10.1029/2019JE005979.

[31]   M. Limpinsel, "Iron Pyrite Absorbers for Solar Photovoltaic Energy Conversion," IRVINE, 2015.

[32]   L. Luo, W. Luan, B. Yuan, C. Zhang, and L. Jin, "High Efficient and Stable Solid Solar Cell: Based on FeS2 Nanocrystals and P3HT: PCBM," *Energy Procedia*, vol. 75, Aug. 2015, doi: 10.1016/j.egypro.2015.07.368.

[33]   M. Law, "Pyrite Iron Sulfide Solar Cells Made from Solution," Irvine, 2017.

[34]   G. Willeke, O. Blenk, Ch. Kloc, and E. Bucher, "Preparation and electrical transport properties of pyrite (FeS2) single crystals," *Journal of Alloys and Compounds*, vol. 178, no. 1–2, Feb. 1992, doi: 10.1016/0925-8388(92)90260-G.

[35]   X. Zhang *et al.*, "Potential resolution to the doping puzzle in iron pyrite: Carrier type determination by Hall effect and thermopower," *Physical Review Materials*, vol. 1, no. 1, Jun. 2017, doi: 10.1103/PhysRevMaterials.1.015402.

[36]   S. W. Lehner, K. S. Savage, and J. C. Ayers, "Vapor growth and characterization of pyrite (FeS2) doped with Co, Ni, and As: Variations in semiconducting properties," *Journal of Crystal Growth*, vol. 286, no. 2, Jan. 2006, doi: 10.1016/j.jcrysgro.2005.09.062.

[37]   R. Sun, M. K. Y. Chan, S. Kang, and G. Ceder, "Intrinsic stoichiometry and oxygen-induced p-type conductivity of pyrite FeS2," *Physical Review B*, vol. 84, no. 3, Jul. 2011, doi: 10.1103/PhysRevB.84.035212.

[38]   E. Mellikov, J. Hiie, and M. Altosaar, "Powder materials and technologies for solar cells," *International Journal of Materials and Product Technology*, vol. 28, no. 3/4, 2007, doi: 10.1504/IJMPT.2007.013082.

[39]   F. Ghisani *et al.*, "Synthesis and characterization of tetrahedrite Cu10Cd2Sb4S13 monograin material for photovoltaic application," *Materials Science in Semiconductor Processing*, vol. 110, May 2020, doi: 10.1016/j.mssp.2020.104973.

[40] M. Kauk-Kuusik *et al.*, "Study of Cu2CdGeSe4 monograin powders synthesized by molten salt method for photovoltaic applications," *Thin Solid Films*, vol. 666, Nov. 2018, doi: 10.1016/j.tsf.2018.09.025.

[41] Adegoke John, "COMPARITIVE STUDY OF Cu2ZnSnSe4 MONOGRAIN POWDER SYNTHESIS IN DIFFERENT MOLTEN FLUXES," Tallinn, 2015.

[42] E. Mellikov *et al.*, "Monograin materials for solar cells," *Solar Energy Materials and Solar Cells*, vol. 93, no. 1, Jan. 2009, doi: 10.1016/j.solmat.2008.04.018.

[43] M. Limpinsel *et al.*, "An inversion layer at the surface of n-type iron pyrite," *Energy & Environmental Science*, vol. 7, no. 6, 2014, doi: 10.1039/c3ee43169j.

[44] J. D. Myers *et al.*, "Reduction in surface state defects in iron pyrite by use of zinc sulfide passivation layers," *Optical Materials Express*, vol. 8, no. 12, Dec. 2018, doi: 10.1364/OME.8.003835.

[45] F. Schindler *et al.*, "Towards the efficiency limits of multicrystalline silicon solar cells," *Solar Energy Materials and Solar Cells*, vol. 185, pp. 198–204, Oct. 2018, doi: 10.1016/j.solmat.2018.05.006.

[46] C. Leiner, F. P. Wenzl, C. Sommer, and G. Peharz, "Improving the effectiveness of photovoltaic devices by light guiding optical foils," Sep. 2016. doi: 10.1117/12.2237866.

[47] H.-M. Song and J. I. Zink, "EELS Study of Differential Diffusion of Fe and Co in Magnetized Silica Nanocomposites," *The Journal of Physical Chemistry C*, vol. 120, no. 44, Nov. 2016, doi: 10.1021/acs.jpcc.6b07264.

[48] ScholAR Chemistry, "Material Safety Data Sheet Potassium Iodide ," Henrietta Rd, Rochester, NY, 2008.

[49] Parasuraman Swaminathan, "Metal-semiconductor junctions," in *NOC: Fundamentals of electronic materials and devices*, 2017.

[50] L. Wu *et al.*, "Enhanced Photoresponse of FeS2 Films: The Role of Marcasite-Pyrite Phase Junctions," *Advanced Materials*, vol. 28, no. 43, Nov. 2016, doi: 10.1002/adma.201602222.

[51] W. M. H. Sachtler, G. J. H. Dorgelo, and A. A. Holscher, "The work function of gold," *Surface Science*, vol. 5, no. 2, pp. 221–229, Oct. 1966, doi: 10.1016/0039-6028(66)90083-5.

[52] D. S. M. B. T. O. S. S. H. H. P. S. P. C. M. H. C. M. M. Berg, "Work function of Pt thin films with disorder," *APS March Meeting*, 2018.

[53] D. Titus, E. James Jebaseelan Samuel, and S. M. Roopan, "Nanoparticle characterization techniques," in *Green Synthesis, Characterization and Applications of Nanoparticles*, Elsevier, 2019, pp. 303–319. doi: 10.1016/b978-0-08-102579-6.00012-5.

[54] D. Wolverson, "Raman spectroscopy," in *Characterization of Semiconductor Heterostructures and Nanostructures*, Elsevier, 2008, pp. 249–288. doi: 10.1016/B978-0-444-53099-8.00008-7.

[55] A. Axelevitch and G. Golan, "Hot-probe method for evaluation of majority charged carriers concentration in semiconductor thin films," *Facta universitatis - series: Electronics and Energetics*, vol. 26, no. 3, 2013, doi: 10.2298/FUEE1303187A.

[56] Ossila enabling materials science, "Measuring and Analysing an I-V Curve," *https://www.ossila.com/pages/iv-curves-measurement (retrieved 17.02.2021)*.

[57] Evaluation Engineering, "Fundamentals of Semiconductor C-V Measurements," *https://www.evaluationengineering.com/home/article/13003970/fundamentals-of-semiconductor-cv-measurements (retrieved 27.04.2021)*, Dec. 2008.

[58] J. S. Moya, C. Baudín, and P. Miranzo, "Sintering," in *Encyclopedia of Physical Science and Technology*, Elsevier, 2003, pp. 865–878. doi: 10.1016/B0-12-227410-5/00694-3.

[59] R. Steudel, "Liquid Sulfur ," *Topics in Current Chemistry*, vol. 230, 2003, doi: 10.1007/b12111.

[60] Y. , F. M. , Y. T. Sato, "Viscosities of Molten Alkali-Metal Bromides and Iodides," *International Journal of Thermophysics,* vol. 18, no. 5, 1997.

[61] E. V. Korolev, V. A. Smirnov, and A. V. Evstigneev, "Nanostructure of matrices for sulfur constructional composites: methodolody, Methods and research tools," *Nanotechnologies in Construction: A Scientific Internet-Journal*, vol. 6, no. 6, Dec. 2014, doi: 10.15828/2075-8545-2014-6-6-106-148.

[62] R. H. Lara, M. G. Monroy, M. Mallet, M. Dossot, M. A. González, and R. Cruz, "An experimental study of iron sulfides weathering under simulated calcareous soil conditions," *Environmental Earth Sciences*, vol. 73, no. 4, Feb. 2015, doi: 10.1007/s12665-014-3540-y.

[63] D. Petrov, "Possibilities of the laser 'Raman' spectroscopy to study the zonal, polymorphic and with elements-impurities ore minerals," *Topical Issues of Rational Use of Natural Resources*, Apr. 2016.

[64] X. Yuan and H. Zheng, "In situ Raman spectroscopic studies of FeS2 pyrite up to 675 K and 2100 MPa using a hydrothermal diamond anvil cell," *Mineralogical Magazine*, vol. 79, no. 1, Feb. 2015, doi: 10.1180/minmag.2015.079.1.01.

[65] G. Han, S. Su, Y. Huang, W. Peng, Y. Cao, and J. Liu, "An Insight into Flotation Chemistry of Pyrite with Isomeric Xanthates: A Combined Experimental and Computational Study," *Minerals*, vol. 8, no. 4, Apr. 2018, doi: 10.3390/min8040166.

[66] M. D. Yuniati, T. Hirajima, H. Miki, and K. Sasaki, "Silicate Covering Layer on Pyrite Surface in the Presence of Silicon-Catechol Complex for Acid Mine Drainage Prevention," *MATERIALS TRANSACTIONS*, vol. 56, no. 10, 2015, doi: 10.2320/matertrans.M-M2015821.

APPENDIX

Article published at the International Astronautical Congress

IAC-20-C3.4.10 (x56905)

Monograin layer solar cell for future lunar outpost

Katriin Kristmann[a], Mare Altosaar[a], Jaan Raudoja[a], Maarja Grossberg[a], Jüri Krustok[a,b], Taavi Raadik[a*]

[a] *Department of Materials and Environmental Technology, Tallinn University of Technology, Ehitajate Tee 5, 19086, Tallinn, Estonia*

[b]*Division of Physics, Tallinn University of Technology, Ehitajate tee 5, 19086 Tallinn, Estonia*

taavi.raadik@taltech.ee

* Corresponding Author

Abstract

One of the most important issues in establishing a lunar outpost will be the availability of energy sources. Using solar PV panels enables permanent electricity production due to the constant illumination by sunlight near the lunar South Pole, that is selected as a future lunar outpost location. Instead of transporting solar panels from Earth, it would be more perspective to find a way to produce them *in situ* on the Moon from the resources available in lunar regolith. The monograin layer solar cell technology enables to manufacture flexible, lightweight and cost-efficient solar panels to cover vast areas with minimum cost. In the current paper we report the development of molten salt synthesis of FeS_2 microcrystals for monograin layer solar cell absorber from elements available in the lunar regolith. We have been successful in syntheses of FeS_2 microcrystals with desired size around 50 microns. The present study is part of an ongoing research.

Keywords: monograin layer solar cell, molten salt synthesis, FeS_2, in-situ resource utilization, lunar base

Acronyms/Abbreviations

EDX   Energy-dispersive X-ray

             spectroscopy

HR-SEM   High resolution scanning electron
             microscope

ISRU   In-Situ Resources Utilization

MGL   monograin layer

TCO   transparent conductive oxide

KI   potassium iodide

XRD   X-ray diffraction

1. Introduction

Establishing a Moon village will be the first step towards future planetary space flights and learning to manage with available resources is a key in the success of these missions [1,2]. One of the important issues in establishing a lunar outpost will be the availability of energy sources. Using solar energy is promising as some areas on lunar south pole, that are selected as a future Moon base location, are constantly illuminated by the Sun. Producing solar panels *in situ* from elements of lunar regolith would be the best use of available resources, but the need to release and purify the materials for solar cells from lunar regolith is a huge technological challenge. Nevertheless, lunar *In-Situ*

Resource Utilization (ISRU) is the key direction by many space agencies and private sector - that's why intensive work is in progress to develop technology for different disciplines. Aim is to use Moon´s resources to produce water, rocket fuel, building materials, any other supplies and harvest energy, in order to achieve as much independence as possible form the supply missions from earth, because resupply missions are expensive and time consuming [3]. As already mentioned before, one of the most important issues to keep lunar outpost on the run, is energy and therefore the energy harvesting from the sunlight is one of the most promising option. When setting up the outpost it is obvious that first solar panels are brought from the earth, but with the outpost growth there is need for the technology to produce them *in situ*. One promising possibility is to use the monograin layer (MGL) solar cell technology [4–6]. The monograin layer (MGL) solar cell concept for semiconductor compounds was proposed more than 50 years ago by researchers of the Philips Company [7], additional developments, modifications and patents were taken by the TalTech researchers and crystalsol GmbH. The MGL solar cell has a superstrate solar cell structure: *graphite/absorber/buffer/TCO/substrate* (glass or polymer film), where the absorber is a monolayer of nearly unisize, with a typical diameter of 50 µm, semiconductor powder crystals embedded into a layer of epoxy (Figure 1.) [8]. MGL technology is completely different from traditional crystalline or thin film solar cell technologies. MGL lightweight solar panel technology

combines the advantages of high-efficient single-crystalline material and low-cost roll-to-roll panel production, enabling to manufacture flexible, lightweight, and cost-efficient solar panels from powders of crystalline semiconductor absorber material. MGL technology allows to cover vast areas with minimum cost [4]. As every semiconductor particle in this powder is coated with an extremely thin buffer layer for creating the p/n junction it is already a tiny photovoltaic cell. Therefore, the MGL technology has an advantage compared to all thin film technologies because it allows to separate powder production from module finishing. Lightweight flexible solar cell module rolls can be transported to the Moon villages or produced *in situ* from lunar regolith. Due to the MGL solar cell advantages European Space Agency has shown remarkable interest to the technology. In order to evaluate the suitability of MGL technology to the space applications Raadik *et. al* [9] has carried out the preliminary environment tests with semi-finished MGL solar cells based on kesterite absorber crystals, in simulated lunar environment. The results of preliminary tests were promising to practise the technology for extra-terrestrial usage.

Fig. 1. Left schematic of MGL solar cell [8], right semi-finished MGL solar cell without encapsulant

The word "regolith" is a terrestrial term, also used for describing the Moon's soil. Apollo missions found that the regolith composition is a bit different on the Moon mare and highland regions. Soils from mare areas have an overall basaltic composition with a high Fe content, while the highland soils have high Al and Ca values. The major elements are O, Na, Mg, Al, Si, Fe, Ca, Ti and S [10]. The amounts of other elements are smaller, such as K, I, Zn; however most of the elements that are present in Earth can be also found from the Moon [11,12]. Therefore, we can harvest most of the necessary elements for solar cell production *in situ* from the lunar soil, starting from absorber layer and ending up at antireflection surface coating. The playground for combining different elements for finding the suitable semiconductor is relatively vast.

One promising candidate for MGL solar cell absorber material is pyrite (FeS_2). Pyrite is a semiconductor material that has all necessary parameters to become the most promising solar cell material for the lunar base purpose. Pyrite has a suitable bandgap of 0.95 eV, high absorption coefficient, high minority carrier diffusion length and an electron mobility up to 360 $cm^2V^{-1}s^{-1}$ at room temperature - all making pyrite attractive as an absorber material to achieve potentially up to 30% power conversion efficiency [13]. It is necessary to extract iron and sulphur from regolith to manufacture pyrite (FeS_2). According to literature, iron as element exists in lunar soil in large quantities in the form of silicate and oxide phases. Troilite (FeS) can also be found in the Moon regolith, only addition of sulphur is required to form pyrite (FeS_2). It has been reported that sulphur can

be extracted from regolith by heating it at 750-1100°C [14,15]. In the current paper we will not focus on the problem how to extract necessary elements from regolith but solely on the technological steps required to produce absorber material for monograin layer solar cells from elements, which are available in regolith.

2. Materials and methods

2.1 Synthesis of FeS$_2$ microcrystals

FeS$_2$ microcrystals were synthesized and grown in a two-step process from binary compound FeS (Alpha Aesar, 3N purity) and elemental S (3N purity) in the liquid phase of S (first step) and recrystallized in KI (second step). Amount of S for synthesis was weighted considering that a part of it is consumed in the reaction to form FeS$_2$ and another part for formation of liquid phase (flux) at the used synthesis temperatures, at 500, 550 and 600 °C. The temperatures were chosen according to the phase diagrams of iron-sulphur system [16,17], in order to stay in the pyrite phase region. The volume of liquid flux (V$_L$) (in both cases, S and KI) and the volume of solid FeS$_2$ (V$_S$) should be approximately equal as necessary for monograin growth [18]. The mixtures were sealed into evacuated quartz ampoules and heated in furnace for one week at temperatures as stated before, after that, the process was stopped by quenching the ampoules in water. Samples were removed from S flux by sublimation in vacuum at 125 °C. Afterwards the samples prepared at 500, 550 and 600 °C were removed from the

excess of sulphur by leaching the samples with KCN water solution. As the FeS$_2$ crystals released from S were too small for preparation of monograin membranes, the crystals synthesised at 600 °C were recrystallized in KI flux at 740 °C for one week to produce bigger grains. The ampoule with recrystallized powder was cooled in the furnace from 740 to 575 °C slowly to ensure the phase transition of FeS$_2$ from pyrrhotite to pyrite [16]. The furnace was kept at 575°C for 24 hours, after that the ampoule was rapidly cooled by quenching in water. For releasing FeS$_2$ crystals from solid KI-flux, deionised water was used.

2.2 Characterization of FeS$_2$ microcrystals

The phase composition of the synthesized FeS$_2$ powders was studied by XRD and by Raman spectroscopy using the Horiba's LabRam HR800 spectrometer equipped with a multichannel CCD detection system in the backscattering configuration. 532 nm laser line with spot size of 5 mm was used for excitation. The chemical composition of powders was determined by energy dispersive X-ray spectroscopy (EDX) using Bruker Esprit 1.8 system. The morphology of crystals was studied with the high-resolution scanning electron microscope (HR-SEM) Zeiss ULTRA 55. EDX mapping was performed over the polished crystals surface to investigate the elemental distribution and compositional uniformity of different microcrystals. X-ray diffraction (XRD) patterns were recorded on a Rigaku Ultima IV diffractometer with Cu K$_\alpha$ radiation (λ=1.5406 Å). PDXL 2 software was used for

the derivation of crystal structure information from the recorded XRD data.

4. Results and Discussion

4.1 Synthesis of FeS_2 crystals in S as a flux

In the first step FeS_2 was synthesized in the medium of liquid sulphur functioning as a flux. The surface morphology and shape of the synthesized crystals were characterized by SEM (see Fig. 2, 3, 4). As it can be seen in Figure 2 the FeS_2 crystals grown at 500 °C are not formed yet as single crystals, they consist of small particles sintered together.
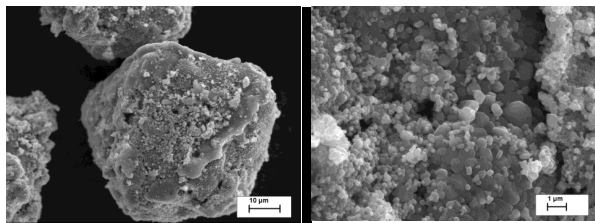
Fig. 2. SEM images of FeS_2 particles (left) and crystals' surfaces (right) grown in S as flux at 500 °C

Microcrystals synthesised at 550 °C (see Fig. 3) have smoother surfaces, nevertheless the big conglomerates sintered together from smaller crystals can still be seen. The average size of individual crystallites is around 1 μm.

In order to grow bigger crystals in sulphur, the crystals' synthesis-growth at 600 °C was preformed, nevertheless there were no big differences in size and morphology if to compare crystals from syntheses made at 550 °C and 600 °C (see Fig. 3 and Fig. 4). To grow bigger crystals there are two options, whether to increase time or temperature. As can be noticed, the growth at 600 °C resulted in slightly bigger crystals therefore we decided to increase the temperature further. As sulphur was found not to be the best flux material, because the removal of it from the microcrystals' surface via sublimation and/or KCN etching are both time consuming processes. A big disadvantage of using sulphur as a flux in large-scale production of FeS_2 is the need to remove it by leaching with KCN solution that produces vast amount of toxic wastewater that is not sustainable in a longer perspective. Therefore we looked for a more suitable flux material with melting point at around 700 °C. KI seemed to be the best option to use as flux material, because its melting point is 681 °C, it is a very stable compound and will not react with precursors [19], it is also water soluble.
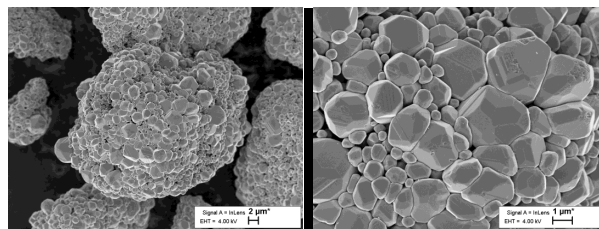

Fig. 3. SEM images of FeS_2 synthesized at 550 °C in S flux

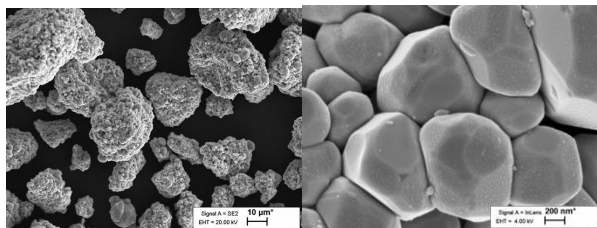Fig. 4. SEM images of FeS$_2$ synthesized at 600 °C in S flux

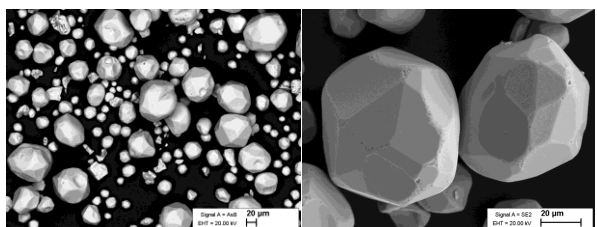### 4.2 Recrystallization of FeS$_2$ crystals in KI flux

Fig. 5. SEM images of FeS$_2$ crystals grown in KI flux at 740 °C

KI has been used as flux in syntheses of different absorber materials for MGL solar cells: kesterites, CIGS and SnS [20–22]. The melting temperature of KI (681 °C) is lower than the decomposition temperature of FeS$_2$ into pyrrhotite and sulphur (744 °C) [17] and the presence of its liquid phase in amount providing $V_L > 0.6\ V_S$ enhances the growth of separate individual grains of FeS$_2$ and inhibits the formation of agglomerates [5].

The FeS$_2$ powder synthesized in liquid sulphur at 600 °C (see the previous chapter) was recrystallized in KI as flux at 740 °C for one week. Formed crystals had a nice uniform shape and smooth surfaces (see Fig. 5). Roughly half of the gained powder material

was in the desired fraction size of around 50 microns.

4.3 Raman, EDX and XRD results

Raman spectra of microcrystals synthesized in sulphur at different temperatures can be seen in figures 6, 7, 8 and that of recrystallized in KI is presented in Fig. 9. Raman peaks at 343, 350, 379 and a weak peak at 430 cm^{-1} (Figures 8 and 9) are characteristic to the pyrite phase as reported in the literature [23,24]. Secondary phases present along with pyrite can be identified by Raman peaks: at 216 and 219 cm^{-1} (Fig. 7) as characteristic to hematite (Fe$_2$O$_3$) [25] (in synthesis at 550 °C) and at 474 cm^{-1} (Fig. 6, 8) as characteristic to elemental sulphur [26] (in syntheses at 500 °C and 600 °C). Deciding on the base of Raman analysis the purest pyrite phase is formed in recrystallisation of FeS$_2$ powder at 740 °C in KI followed by slow cooling to 575 °C (Figure 9). A slight variation in FeS$_2$ Raman peak positions can be seen in the Raman spectra of samples synthesised at 500 °C and 550 °C and post-annealed in vacuum for sulphur sublimation. The shift in Raman peaks positions could be related with removal of sulphur from the utmost surface layer of FeS$_2$ crystals causing the formation of S-deficient surface layer with variable composition. The shift in Raman peak positions via the formation of solid solutions is well-known [27] . On the base of Raman analysis we can conclude that it is possible to avoid the formation of secondary unwanted iron sulphide phases if to proceed at higher temperatures, provide the conditions for

phase transformation, quench the material quickly and use a flux material that does not require vacuum sublimation or etching for removal [17].
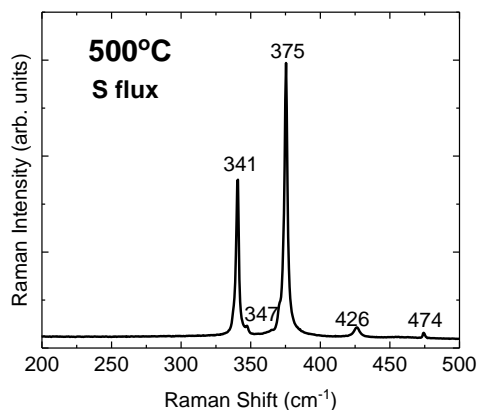

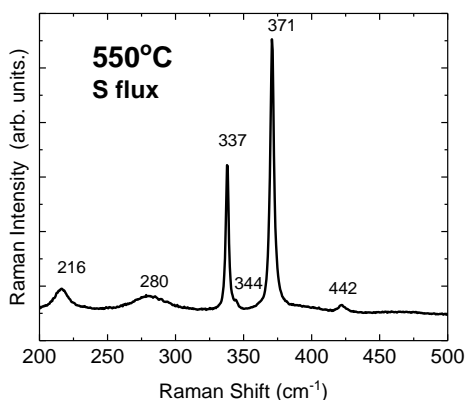Fig. 6. Raman spectrum of crystals synthesized at 500 °C in S flux

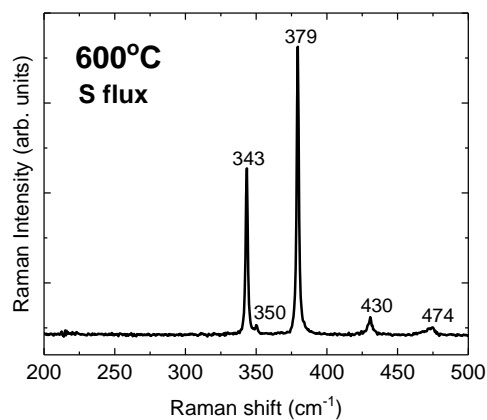Fig. 7. Raman spectrum of crystals synthesized at 550 °C in S flux

Fig. 8. Raman spectrum of crystals synthesized at 600 °C in S flux
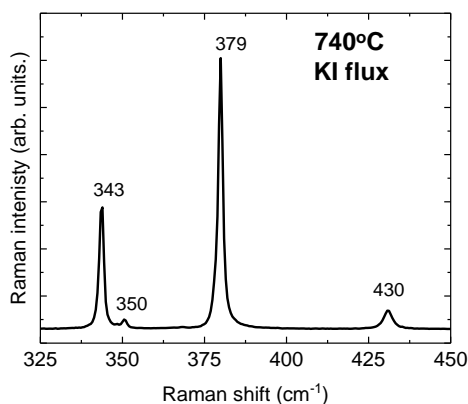

Fig. 9 Raman spectrum of crystals recrystallized at 740 °C in KI flux

According to the EDX results (see Table 1), crystals grown at 500 °C have an iron rich composition of 39.21 at. % iron and 60.79 at. % sulphur. The composition shifts to more stoichiometric side with increasing growth temperature: crystals synthesized at 550 °C

and 600 °C are closer to the stoichiometric composition of pyrite as can be seen in Table 1. Crystals recrystallized at 740 °C had composition of 33.71 at. % iron and 66.29 at. % sulphur. There were no differences weather the composition was measured from the surface or from the bulk. Even though EDX analyses showed almost stoichiometric composition to the 550 °C and 600 °C, there were still some additional phases and elemental sulphur that was confirmed by Raman.

Fig. 10. XRD pattern of crystals recrystallized at 740 °C in KI flux.

Table 1. Composition of crystals grown at different temperatures, determined by EDX

Sample	Fe	S	Fe/S
500°C in S	39.21	60.79	0.65
550°C in S	33.06	66.94	0.49
600°C in S	33.42	66.58	0.50
740°C in KI	33.71	66.29	0.51

Finally, the microcrystals recrystallized at 740 °C were analysed by XRD, the pattern can be seen in Figure 10. The values of lattice parameters a = b = c = 5.4154 Å were recorded, confirming the cubic structure and are in good accordance with values reported in the literature [28–30]. Additionally, XRD supports the Raman results that there are no secondary phases in the crystals recrystallized at 740 °C in KI flux.
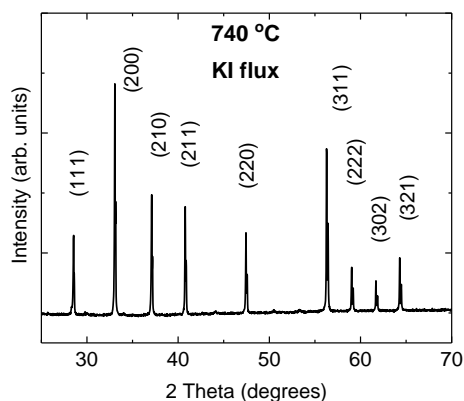
4.4 Monograin layer membrane fabrication

For the preparation of monograin layer membrane the FeS_2 powder recrystallized in KI was sieved and the unisize crystals were used for the monograin membrane formation. Overview and cross-sectional view of the FeS_2 monograin membrane are presented in Fig. 11. As it can be seen from the top view of the membrane in Figure 11 (left side), the crystals have formed relatively dense layer, the packing density is around 70% (area that is covered by crystals). The shape of the crystals allows to achieve packing factor around 85 %. From the cross-sectional view of the membrane (Figure 11, right), it can be seen that the membrane is formed on a supportive flexible foil covered with an epoxy layer in which crystals are embedded so that the upper side of crystals is outside of (and not contaminated by) epoxy and can work as active absorber material if exposed to sun light.
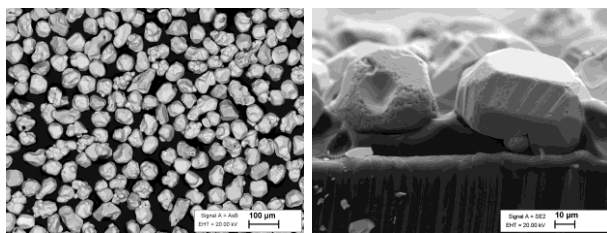
Fig. 11. Overview of FeS_2 monograin layer membrane (left) and cross-sectional view (right)

6. Conclusions

In this work the conditions for synthesis and growth of FeS_2 microcrystalline powders were found. FeS_2 synthesized in sulphur and recrystallized in molten KI as flux had cubic structure with lattice parameters a = b = c = 5.4154 Å characteristic to the pyrite phase of FeS_2. Raman analysis (supported by XRD data) confirmed the pure pyrite phase. The powder crystals had smooth surfaces and proper size for making membranes for monograin membrane solar cells. We found the temperature regime for the growth of FeS_2 microcrystals and a cooling procedure for retaining the pyrite phase of FeS_2 without formation of additional phases that could be detrimental to the solar cell. Next steps will be the finding of the buffer layer material for p-n junction formation preferably also from elements present in lunar regolith. Finally, testing solar cells reliability under artificial lunar environment.

Acknowledgements

References

[1] M. Braun, N.G. Veronica Trivino, S. Hosseini, R. Schonenborg, M. Landgraf, Human lunar return: An analysis of human lunar exploration scenarios within the upcoming decade, Acta Astronaut. (2020). https://doi.org/10.1016/j.actaastro.2020.03.037.

[2] J.N. Rasera, J.J. Cilliers, J.A. Lamamy, K. Hadler, The beneficiation of lunar regolith for space resource utilisation: A review, Planet. Space Sci. (2020). https://doi.org/10.1016/j.pss.2020.104879.

[3] N.J. Bennett, D. Ellender, A.G. Dempster, Commercial viability of lunar In-Situ Resource Utilization (ISRU), Planet. Space Sci. (2020). https://doi.org/10.1016/j.pss.2020.104842.

[4] M. Altosaar, A. Jagomägi, M. Kauk, M. Krunks, J. Krustok, E. Mellikov, J. Raudoja, T. Varema, Monograin layer solar cells, in: Thin Solid Films, 2003. https://doi.org/10.1016/S0040-6090(03)00167-6.

[5] E. Mellikov, D. Meissner, T. Varema, M. Altosaar, M. Kauk, O. Volobujeva, J. Raudoja, K. Timmo, M. Danilson, Monograin materials for solar cells, Sol. Energy Mater. Sol. Cells. (2009). https://doi.org/10.1016/j.solmat.2008.04.018.

[6] E. Mellikov, M. Altosaar, M. Kauk-Kuusik, K. Timmo, D. Meissner, M. Grossberg, J. Krustok, O. Volobujeva, Growth of CZTS-Based Monograins and Their Application to Membrane Solar Cells, in: Copp. Zinc Tin Sulfide-Based Thin-Film Sol. Cells, 2015.

https://doi.org/10.1002/9781118437865.ch13.

[7] G.W.M.. van H. T.S. de Velde, No Title, Philips Techn. Rev. 29 (1968) 238.

[8] C. Leiner, C. Sommer, V. Satzinger, L. Plessing, G. Peharz, CPV membranes made by roll-to-roll printing: A feasible approach?, in: AIP Conf. Proc., 2016. https://doi.org/10.1063/1.4962100.

[9] T. Raadik, Adapting Crystalsol product to a moon environment, ESA GSTP Small Stud. (2016). https://www.esa.int/Enabling_Support/Space_Engineering_Technology/Shaping_the_Future/Adapting_Crystalsol_product_to_a_moon_environment.

[10] D.E. Wilhelms, Lunar stratigraphy and sedimentology, Icarus. (1977). https://doi.org/10.1016/0019-1035(77)90020-3.

[11] G.A. Landis, Materials refining on the Moon, Acta Astronaut. (2007). https://doi.org/10.1016/j.actaastro.2006.11.004.

[12] J.M.D. Day, E.M.M.E. van Kooten, B.A. Hofmann, F. Moynier, Mare basalt meteorites, magnesian-suite rocks and KREEP reveal loss of zinc during and after lunar formation, Earth Planet. Sci. Lett. (2020). https://doi.org/10.1016/j.epsl.2019.115998.

[13] M. Rahman, G. Boschloo, A. Hagfeldt, T. Edvinsson, On the Mechanistic Understanding of Photovoltage Loss in Iron Pyrite Solar Cells, Adv. Mater. (2020). https://doi.org/10.1002/adma.201905653.

[14] R. V. Morris, Origins and size distribution of metallic iron particles in the lunar regolith., Geochim. Cosmochim. Acta, Suppl. (1980).

[15] D. Vaniman, D. Pettit, G. Heiken, Uses of lunar sulfur, in: 2nd Conf. Lunar Bases Sp. Act., 1992.

[16] O.K. von Goldbeck, IRON—Binary Phase Diagrams, 1982. https://doi.org/10.1007/978-3-662-08024-5.

[17] D. Shishin, E. Jak, S.A. Decterov, Critical Assessment and Thermodynamic Modeling of the Fe-O-S System, J. Phase Equilibria Diffus. (2015). https://doi.org/10.1007/s11669-015-0376-4.

[18] M. Altosaar, E. Mellikov, CuInSe 2 Monograin Growth in CuSe-Se Liquid Phase , Jpn. J. Appl. Phys. (2000). https://doi.org/10.7567/jjaps.39s1.65.

[19] I. Leinemann, K. Timmo, M. Grossberg, T. Kaljuvee, K. Tõnsuaadu, R. Traksmaa, M. Altosaar, D. Meissner, Reaction enthalpies of Cu2ZnSnSe4 synthesis in KI, J. Therm. Anal. Calorim. (2015). https://doi.org/10.1007/s10973-014-4339-5.

[20] M. Altosaar, J. Raudoja, K. Timmo, M. Danilson, M. Grossberg, M. Krunks, T. Varema, E. Mellikov, Cu2ZnSnSe4 monograin powders for solar cell application, in: Conf. Rec. 2006 IEEE 4th World Conf. Photovolt. Energy Conversion, WCPEC-4, 2006. https://doi.org/10.1109/WCPEC.2006.279492.

[21] K. Timmo, M. Kauk-Kuusik, M. Pilvet, M. Altosaar, M. Grossberg, M. Danilson, R. Kaupmees, V. Mikli, J. Raudoja, T. Varema, Cu(In,Ga)Se2 monograin powders with different Ga content for solar cells, Sol. Energy. (2018). https://doi.org/10.1016/j.solener.2018.10.078.

[22] K. Timmo, M. Kauk-Kuusik, M. Pilvet, V. Mikli, E. Kärber, T. Raadik, I. Leinemann, M. Altosaar, J. Raudoja, Comparative study of SnS recrystallization in molten CdI2, SnCl2and KI, Phys. Status Solidi Curr. Top. Solid State Phys. (2016). https://doi.org/10.1002/pssc.201510082.

[23] H. Vogt, T. Chattopadhyay, H.J. Stolz, Complete first-order Raman spectra of the pyrite structure compounds FeS2, MnS2 AND SiP2, J. Phys. Chem. Solids. (1983). https://doi.org/10.1016/0022-3697(83)90124-5.

[24] A.N. Utyuzh, Influence of temperature on raman spectra of the FeS2 single crystal with pyrite structure, Phys. Solid State. (2014). https://doi.org/10.1134/S1063783414100321.

[25] D.L.A. De Faria, S. Venâncio Silva, M.T. De Oliveira, Raman microspectroscopy of some iron oxides and oxyhydroxides, J. Raman Spectrosc. (1997). https://doi.org/10.1002/(sici)1097-4555(199711)28:11<873::aid-jrs177>3.0.co;2-b.

[26] A.T. Ward, Raman spectroscopy of sulfur, sulfur-selenium, and sulfur-arsenic mixtures, J. Phys. Chem. (1968). https://doi.org/10.1021/j100858a031.

[27] M. Grossberg, J. Krustok, J. Raudoja, K. Timmo, M. Altosaar, T. Raadik, Photoluminescence and Raman study of Cu2ZnSn(Se xS1 - X)4 monograins for photovoltaic applications, in: Thin Solid Films, 2011. https://doi.org/10.1016/j.tsf.2010.12.099.

[28] A. Zavrazhnov, A. Naumov, A. Kosyakov, S. Berezin, V. Volkov, A. Sergeeva, The Iron Sulfides Crystal Growth from the Halide Melts, Mater. Res. (2018). https://doi.org/10.1590/1980-5373-mr-2017-0648.

[29] P. Prabukanthan, S. Thamaraiselvi, G. Harichandran, Single Step Electrochemical Deposition of p-Type Undoped and Co 2+ Doped FeS 2 Thin Films and Performance in Heterojunction Solid Solar Cells , J. Electrochem. Soc. (2017). https://doi.org/10.1149/2.0991709jes.

[30] H. Ning, Z. Liu, Y. Xie, H. Huang, CoS 2 Coatings for Improving Thermal Stability and Electrochemical Performance of FeS 2 Cathodes for Thermal Batteries , J. Electrochem. Soc. (2018). https://doi.org/10.1149/2.0321809jes.

80